Gravity wave instability structures and turbulence from more than one and a half years of OH* airglow imager observations in Slovenia

René Sedlak[1], Patrick Hannawald[1,2], Carsten Schmidt[2], Sabine Wüst[2], Michael Bittner[1,2], and Samo Stanič[3]

[1]Institute of Physics, University of Augsburg, Augsburg, Germany
[2]German Remote Sensing Data Center, German Aerospace Center, Oberpfaffenhofen, Germany
[3]Center for Astrophysics and Cosmology, University of Nova Gorica, Ajdovščina, Slovenia

Correspondence to: René Sedlak (rene.sedlak@physik.uni-augsburg.de)

Abstract. We analysed 286 nights of data from the OH* airglow imager FAIM 3 (Fast Airglow IMager) acquired at Otlica Observatory (45.93 °N, 13.91 °E), Slovenia between 26 October 2017 and 6 June 2019. Measurements have been performed with a spatial resolution of 24 m pixel^{-1} and a temporal resolution of 2.8 s.

A two-dimensional Fast Fourier transform is applied to the image data to derive horizontal wavelengths between 48 m and 4.5 km in the upper mesosphere / lower thermosphere (UMLT) region. In contrast to the statistics of larger scale gravity waves (horizontal wavelength up to ca. 50 km, e.g., Hannawald et al., 2019) we find a more isotropic distribution of directions of propagation, pointing to the presence of wave structures created above the stratospheric wind fields. A weak seasonal tendency of a majority of waves propagating eastward ~~(westward)~~ during winter ~~(summer)~~ may be due instability features from ~~to~~ breaking secondary gravity waves ~~originating from breaking primary waves~~that were created in the stratosphere. We also observe an increased southward propagation during summer, which we interpret as an enhanced contribution of secondary gravity waves created as a consequence of primary wave filtering by the meridional mesospheric circulation.

We present multiple observations of turbulence episodes captured by our high-resolution airglow imager ~~Furthermore, observations of turbulent vortices allowed the estimation~~and estimated ~~of eddy diffusion coefficients~~the energy dissipation rate in the UMLT from image sequences in ~~45~~ 25 cases. Values range around 0.08 and 9.03 W kg^{-1} ~~10^3 – 10^4 m^{2}s^{-1}~~ and ~~mostly agree with~~ are on average higher than those in recent literature. ~~Turbulently dissipated energy is derived taking into account values of the Brunt Väisälä frequency based on TIMED-SABER (Thermosphere Ionosphere Mesosphere Energetics Dynamics, Sounding of the Atmosphere using Broadband Emission Radiometry) measurements as presented by Wüst et al. (2020). Energy dissipation rates range between 0.63 W kg^{-1} and 14.21 W kg^{-1} leading~~The values found here would lead to an approximated localized maximum heating of 0.03 - 3.02 K ~~0.2 – 6.3 K~~ per turbulence event. These are in the same range as the daily chemical heating rates for the entire atmosphere reported by Marsh (2011), which apparently stresses the importance of dynamical energy conversion in the UMLT.

1 Introduction

Fully understanding the contribution of gravity waves to atmospheric dynamics is still a major issue when establishing climate models. Due to the various sources and mechanisms of interactions the effects of gravity waves have to be represented in these models using advanced parameterizations (Lindzen, 1981; Holton, 1983; de la Cámara et al., 2016) to cover as many aspects as it is possible given the restricted model resolution. Gravity waves exist on a large span of time scales ranging from several hours down to the Brunt-Väisälä (BV) period, which corresponds to ca. 4 - 5 min in the upper mesosphere / lower thermosphere (UMLT) region (Wüst et al., 2017b) and represents the smallest possible period of gravity waves. They show diverse behaviour depending strongly on wave properties like their periodicity (Fritts & Alexander, 2003; Beldon & Mitchell, 2009; Hoffmann et al., 2010; Wüst et al., 2016; Sedlak et al., 2020), which makes it even harder to fully account for them by means of parameterization. Furthermore, gravity wave generation is not restricted to the ~~ground~~ troposphere but can also take place at higher altitudes, such as secondary wave excitation due to breaking gravity waves (see, e.g., Holton & Alexander, 1999; Satomura & Sato, 1999; Vadas & Fritts, 2001; Becker & Vadas, 2018).

As Fritts & Alexander (2003) state, it is necessary to metrologically capture all parts of the gravity wave spectrum. This includes especially dynamics on short scales where gravity wave breaking is induced by the development of instabilities. One of the most prominent features in this context is the formation of Kelvin-Helmholtz instability (KHI), which occurs as a consequence of a dynamically instable atmosphere due to wind shear (Browning, 1971). Gravity wave instability can also be of convective nature when growing wave amplitudes lead to a superadiabatic lapse rate (Fritts & Alexander, 2003). In general, atmospheric instabilities like KHIs often manifest as so-called ripples – periodic structures with small spatial dimensions and short lifetimes (Peterson, 1979; Adams et al., 1988; Taylor & Hapgood, 1990; Li et al., 2017).

Gravity wave breaking and the conversion of the transported energy into heat takes place in the course of turbulence. Once a wave breaks and motion shifts from laminar to turbulent flow energy is cascaded to smaller and smaller structures until viscosity becomes dominant over inertia and energy is dissipated into the atmosphere by viscous damping (see, e.g., Lübken et al., 1987).

The process of turbulence manifests as formation of vortices, so-called eddies. They cause turbulent mixing of the medium, ~~which is described by the eddy diffusion coefficient K~~ resulting in the dissipation of turbulent energy at an energy dissipation rate ϵ. According to the theory of stratified turbulence, ϵ depends on the characteristic length scale L and velocity scale U of the turbulent features. The energy dissipation rate is then given by

$$\epsilon K = C_\epsilon \frac{2}{3\pi} \frac{U^3}{L} r_e v_e \quad (1)$$

(see, e.g., Chau et al, 2020; who apply this equation to radar observations of KHIs). C_ϵ is a constant which is found to be equal to 1 (Gargett, 1999). ~~K can be calculated from the eddy radius r_e and the circumferential velocity v_e by~~

~~$$K = \frac{2}{3\pi} r_e v_e \quad (1)$$~~

~~(see e.g. Prölss, 2001. The derivation is outlined in detail in appendix A.). According to Weinstock (1978), knowing K and the BV frequency N, an estimate for the energy dissipation rate ϵ – the rate at which turbulent kinetic energy is dissipated into heat at the short scale end of the energy cascade of the inertial subrange (Li et al., 2016) – can be calculated using~~

~~$$K \approx 0.81 \cdot \left(\frac{\epsilon}{N^2}\right). \quad (2)$$~~

Gravity wave dissipation predominantly occurs in the upper mesosphere / lower thermosphere (UMLT) region (Gardner et al., 2002). Hocking (1985) states that the turbulent regime at this altitude manifests on scales shorter than 1 km, which sets high requirements for measurement techniques at these heights. This is why turbulence investigations in the UMLT are challenging and there are only few values of ~~ϵ, K~~ available at UMLT heights. Lübken et al. (1997) use rocket measurements to retrieve ~~K and ϵ~~ in the height range 65 - 120 km. ~~Liu (2009) presents a method for the estimation of K from gravity wave momentum fluxes derived from lidar data.~~ Baumgarten & Fritts (2014) use imaging techniques of mesospheric noctilucent clouds to investigate the formation of KHIs and the onset of turbulence.

At the same height, remote sensing measurements of the OH* airglow are an established access to UMLT dynamics. The OH* airglow is a layer at an average altitude of ca. 86–87 km with a full width at half maximum (FWHM) of ca. 8 km (Baker & Stair, 1988; Liu & Shepherd, 2006; Wüst et al., 2017b). ~~These~~ Remote sensing techniques include spectroscopic measurements of strong emission lines and the analysis of temperature time series derived from these (Hines & Tarasick, 1987; Mulligan et al., 1995; Bittner et al., 2000; Reisin & Scheer, 2001; Espy & Stegman, 2002; Espy et al., 2003; French & Burns, 2004; Offermann, 2009; Schmidt et al., 2013, 2018, Wachter et al., 2015; Silber et al., 2016, Wüst et al., 2016, 2017a, 2018), but also two-dimensional imaging in the short-wave infrared (SWIR) range (see, e.g., Peterson & Kieffaber, 1973; Hecht et al., 1997; Taylor, 1997; Moreels et al., 2008; Li et al., 2011; Pautet et al., 2014; Hannawald et al., 2016, 2019; Sedlak et al., 2016; Wüst et al., 2019 and many more).

The technology of OH* imaging has undergone a rapid technical progress over the last few decades. ~~Proceedings~~ Improvements in sensor technology and optics have provided the possibility to observe the signatures of gravity waves that manifest as periodic brightness variations in infrared images of the OH* airglow layer. The observations range from all-sky imaging of large-scale gravity waves (e.g., Taylor et al., 1997; Smith et al., 2009) to high resolution images of smaller gravity waves (Nakamura et al., 1999) and their breaking processes (Hecht et al., 2014; Hannawald et al., 2016). Hannawald et al. (2016) use an airglow imager called FAIM (Fast Airglow IMager) that is well-suited for the observation of small-scale gravity waves with a high temporal resolution of 0.5 s. Based on three years of continuous night-time observations at two different Alpine locations Hannawald et al. (2019) show statistics of gravity wave propagation for waves with horizontal wavelengths smaller than 50 km based on data of the same kind of instrument.

In 2016 we put into operation another FAIM instrument (FAIM 3) which still has a high temporal resolution of 2.8 s, but also a high spatial resolution of up to 17 m pixel^{-1} (measurements in zenith direction utilizing a 100 mm SWIR objective lens). We were not only able to observe wave patterns on extraordinary small scales (smallest horizontal wavelength 550 m) but also the formation of a vortex which we interprete as the turbulent breakdown of a wave front (Sedlak et al., 2016).

From October 2017 to June 2019 the instrument observed the area around the Gulf of Trieste from Otlica Observatory, Slovenia (45.93 N, 13.91 °E), which is a partner observatory within the context of the Virtual Alpine Observatory (VAO; https://www.vao.bayern.de). This larger data basis includes further observations of small-scale wave features and turbulence which are investigated here.

The focus of this paper is on analysing small-scale dynamics in the UMLT region in FAIM 3 images with regard to two aspects:

1. A statistical analysis of wave parameters on scales below 4.5 km using a 2-dimensional Fast Fourier Transform (2d-FFT). Using the same measurement technique and analysis we are able to directly connect to the short-scale end of the investigations performed by Hannawald et al. (2019).
2. The estimation of dissipated energy by analyzing multiple episodes of turbulence (such as the one exemplarily presented in Sedlak et al., 2016).

2 Instrumentation

FAIM 3 is an OH* airglow imager that has been put into operation in February 2016 at the German Aerospace Center (DLR) in Oberpfaffenhofen, Germany. It consists of the SWIR camera CHEETAH CL manufactured by Xenics nv, which has a thermodynamically cooled 640 x 512 pixels InGaAs sensor array (pixel size 20 µm x 20 µm, operating temperature 233 K). The camera is sensitive to electro-magnetic radiation in the wavelength range from 0.9 to 1.7 µm (for further technical details see Sedlak et al., 2016).

From 26 October 2017 to 6 June 2019 automatic measurements with focus on the OH* airglow emissions have been performed at Otlica Observatory (OTL) (45.93 N, 13.91 °E), Slovenia. FAIM 3 was aligned at a zenith angle of 35 ° and an azimuthal direction of 240 ° (facing approximately into WSW direction). Measurements are only possible during night-time because OH* emissions are not detectable in the presence of the much stronger solar radiation. A baffle was attached to prevent the images from being disturbed by reflections from the lab interior, e.g., by moon light. As in Sedlak et al. (2016) the camera was equipped with a 100 mm SWIR lens by Edmund Optics® with aperture angles of 7.3 ° and 5.9 ° in horizontal and vertical direction. Neglecting the curvature of the Earth, this configuration leads to a trapezium-shaped field of view (FOV) with a size of ca. 182 km² (13.1 – 14.1 km x 13.4 km) at the mean peak emission height of the OH* layer at ca. 87 km. The mean spatial resolution is therefore 24 m pixel^{-1}. Due to the abovementioned measurement geometry the FOV is located above the Gulf of Trieste. The integration time of FAIM 3 is 2.8 s, which leads, depending on the season, to the acquisition of ca. 10,000 to 18,000 images per night.

3 Data Basis

All in all, in 477 nights image data were acquired by FAIM 3 at OTL. Since OH* airglow observations are only possible under clear sky conditions, cloudy episodes are sorted out by analyzing keograms. This yields 410 clear sky episodes (durations between 20 min and 13 h) that are distributed over 286 measurement nights. Thus, ca. 60 % of the acquired nights at OTL include suitable OH* observations.

Before being analysed, the images undergo the same preprocessing steps as in Hannawald et al. (2016, 2019) and Sedlak et al. (2016): a flat-field correction is performed and the images are transformed to an equidistant grid, which corresponds to a trapezium-shaped FOV due to the inclination from zenith. For each episode the average image is subtracted to ensure that all remnants of fixed patterns are removed (e.g., reflections of the objective lens in the laboratory window during bright nights). Due to the small FOV of FAIM 3 we renounce the application of a star removal algorithm to avoid an interpolation of too many pixels. In order to extract periodic signatures a two-dimensional Fast Fourier Transform (2d-FFT) is applied to squared cut-outs of each image, so that neither dimension is favored by the analysis. These cut-outs were chosen to have a side length of 406 pixels (equals ca. 9.7 km) as this is the largest possible square fitting into the transformed images. The 2d-FFT is performed on the squared image cut-out as described by Hannawald et al. (2019). A fitted linear intensity gradient is subtracted from the input images and a Hann window is applied during the 2d-FFT to reduce leakage effects. A local maximum filter is applied to automatically find peaks in the spectra and thus plane wave structures, which allows identifying and analyzing single wave events. Zero-padding on the images is used to improve this identification of peaks in the spectra. Hannawald et al. (2019) present a statistical analysis of gravity waves with horizontal wavelengths between 2 and 62 km (with focus on waves with horizontal wavelengths larger than 15 km). With FAIM 3 having a smaller FOV and a higher spatial resolution than the FAIM instrument used therein, we are now able to present statistics of gravity wave parameters that tie in almost seamlessly with the statistics of longer-scale waves of Hannawald et al. (2019): due to the spatial resolution and the FOV size we cover the horizontal wavelength range from 48 m to 4.5 km. Wave structures with horizontal wavelengths of half the FOV size still showed a strong bias toward phases 0 or π. Extensive testing showed that this effect disappeared when lowering the upper wavelength limit to 4.5 km.

Observed wave structures have to meet several quality criteria in order to be considered a wave event. A wave structure has to be present for at least 20 s and has to be found in at least eight images. This is in contrast to Hannawald et al. (2019) who demand wave signatures to be present for at least 120 s and to appear in at least 100 images within this episode, stating that these restrictions specifically filter out many transient and small-scale wave features as they want to focus on larger persistent waves.

Furthermore, FAIM 3 wave events are considered if they have an amplitude of at least 25 % of the maximum observed wave amplitude. Wave structures with this amplitude can just be recognized in the image by the eye. Demanding all the quality criteria mentioned above a total number of 5697 wave events remains. Further restricting these criteria has not significantly

altered the distributions of the wave parameters that are presented in the following. An exemplary event and the respective 2-dimensional spectrum are shown in Figure 1.

We often observe episodes of turbulence in our image series that exhibit the typical dynamics of vortex formation and quasi-chaotic behavior. While the identification of wave structures is done automatically by the 2d-FFT, finding turbulent vortices is done by hand. Turbulent eddy formation can be well recognized by eye when viewing the episodes in the dynamical course of a video sequence. However, the combined effect of these vortices having a certain variety of shapes and sizes, being almost invisible in single images without comparison to preceding or successive images, and causing (compared to other features such as wave fronts) rather small brightness fluctuations in the images hampers strongly the application of image recognition algorithms. For the given data basis ~~45~~ 25 episodes of turbulence with sufficient quality to derive ~~vortex~~ turbulence parameters are found. The dates along with the respective turbulence parameters are summarized in Table 1.

~~For both, gravity wave statistics (section 4.1) and the calculation of the energy dissipation rate (section 4.2) the BV frequency is required, which is adapted from the climatology presented by Wüst et al. (2020). It is based on TIMED-SABER (Thermosphere Ionosphere Mesosphere Energetics Dynamics, Sounding of the Atmosphere using Broadband Emission Radiometry) temperature data and takes into account the seasonal variability of the angular BV frequency. The climatology of the grid point (45 ° N, 10 ° E) is used, which is closest to our FOV. Depending on the day of the year (DoY) the BV frequency is given by~~

~~$$N = 2.20 \cdot 10^{-2} s^{-2} + 0.19 \cdot 10^{-2} s^{-2} \sin\left(\frac{2\pi}{324.51 d} \cdot DoY - 2.02\right) + 0.05 \cdot 10^{-2} s^{-2} \sin\left(\frac{2\pi}{180.00 d} \cdot DoY + 1.61\right). \quad (3)$$~~

~~We use an uncertainty of ± 5 % as according to Wüst et al. (2020) 91 % of their data lie within this range around the harmonic approximation. The BV period is then referred to as $\tau_{BV} = \frac{2\pi}{N}$.~~

4 Results

4.1 Statistics of Wave Parameters

The wave statistics are presented in Figure 2~~Figure 1~~. Please note that we a using the word ‘wave’ for all wave-like structures we find in the images. The question whether these are actual gravity waves is discussed in section 5. ~~For each wave event the individual BV period is calculated based on Eq. (3) and the DoY. Ca. 63 % of the observed wave events have a period longer than the respective BV period and will be referred to as gravity wave events in the following. Their statistical contribution is highlighted in grey in Figure 1.~~

Wave periods range from 21 s to 1498 s (25 min). The median wave period is 359 s (6 min). ~~The median value of gravity wave periods is found at 517 s (8.6 min).~~ The maximum phase speed is ~~17.6~~139.8 m s^{-1} with an average value of ~~7.9~~13.3 m s^{-1} and a standard deviation of ~~3~~10.3 m s^{-1}. As concerns the zonal distribution, ~~50.7~~52.7 % (~~49.3~~47.3 %) of the ~~gravity~~ wave events have an eastward (westward) component (consequently no ~~gravity~~ waves with zonal phase speed zero have been observed) and the mean velocity in eastward (westward) direction is ~~5.4~~9.4 m s^{-1} (~~5.3~~8.2 m s^{-1}) with a standard deviation of ~~3.0~~8.9 m s^{-1} (~~3.1~~7.4 m s^{-}

[1]). We find a small seasonal effect in the distribution of zonal phase speeds: ~~53.8~~56.0% of the waves have an eastward component and ~~46.2~~44.0% a westward component when only considering the winter months December to February while during summer from June to August ~~47.9~~49.5% of the waves have an eastward component and ~~52.1~~50.5% a westward component. In meridional direction ~~44.4~~42.0% (~~53.5~~55.7%) of the gravity wave events have a northward (southward) component and the mean meridional phase speed is ~~4.7~~7.5 $m\,s^{-1}$ (~~5.3~~9.4 $m\,s^{-1}$) in northern (southern) direction with a standard deviation of ~~3.0~~7.1 $m\,s^{-1}$ (~~3.2~~8.7 $m\,s^{-1}$). Events with meridional phase speed zero have not been considered for the mean values.

4.2 Wave Dissipation

To give an impression of the turbulent dynamics we observe, we present four of our turbulence episodes as video supplement. On 16 November 2017, 02:16 UTC, the turbulent breakdown of parts of an extended wave field can be observed (video 1). On 6 December 2017, 00:26 UTC, several fronts seem to be building up and form rotating vortices (video 2). This can be observed even clearer on 14 October 2018, 17:08 UTC, where the residual movement of turbulent features can be well recognized above the general background movement (video 3). On 4 November 2018, 19:18 UTC, breaking wave fronts seem to form rotating structures of nearly cylindrical shape, while these are accompanied by other turbulently moving eddies (video 4).

We estimate the turbulent energy dissipation rate ϵ using equation (1). However, in contrast to Chau et al. (2020) who used radar measurements, we only have horizontal information from our airglow imager. Hecht et al. (2021) demonstrate an approach how to apply equation (1) to purely horizontal airglow imager data, which we adapt to our observations in the following. The characteristic length scale L can be read from the images by measuring the size of the turbulent features. The velocity scale is given by the residual velocity v_{res} of these features. In our observations, they are part of larger instability features, which we assume to be advected by the background wind. We determine v_{res} by reading the actual velocity of the turbulent features and subtracting the background movement v_{bg} in the resulting direction. This is exemplarily shown in Figure 4. The two patches highlighted therein are both moving to the upper right direction but are approaching each other. This helps distinguishing background and residual movement.~~The eddy parameters needed for the calculation of the eddy diffusion coefficient (Eq. 1) are determined manually from the image series of the 45 observations of turbulence. It has to be kept in mind that we are deriving properties of a three-dimensional movement from two-dimensional data.~~

~~We assume the vortices to rotate in a perfect circular shape. The lateral expansion creates the impression of a rotating cylinder. Coherently moving structures give indication of the horizontal velocity vector. Unless the rotational axis is aligned perpendicular to the image plane, the three-dimensional vortex rotation manifests as more than one coherent structure that is moving against or overtaking each other (see e.g. Sedlak et al., 2016; Figure 6 therein). During data inspection we noticed that the orientation of the rotational axis can be aligned in any direction. It tends to be parallel to the image plane when it evolves directly from the crests of a breaking wave. However, we could also observe eddies rotating around an axis aligned almost perpendicular to the image plane. An example of a rotating vortex within a FAIM-3 snapshot on 4 November 2018 at 19:36:41 UTC is displayed in Figure 3a. The rotational axis and the direction of rotation are marked therein and on an actual cylinder (Figure 3b) for clarification. Since it is very difficult to identify a vortex structure in a single picture we have attached~~

~~a video sequence of this episode (Video 1). The vortex radius and velocity are read from the images. Besides measuring the vortex rotation, it has also to be taken care of the overall image: if additional to the eddy movement all structures in the FOV are moving into a common direction, this background motion has to be subtracted. In the example shown above the vortex is advected toward the left corner. The distance between camera and observed vortex is much larger than the expansion of the vortex along the rotation axis so that falsifications arising from different perspectives of the vortices can be neglected. This principle is illustrated in Figure 4. As the vortices are three-dimensional the alignment of the rotational axis should not affect the value of the vortex parameters in the images: it does not matter if the axis is aligned perpendicular, parallel or in any other angle to the image plane, the vortex size will be accessible from the two-dimensional projection of the image assuming circular eddy movement. The same holds for the circumferential velocity since both the radius and the circulation time remain unchanged. However, perfectly circular eddy rotation does not necessarily occur in nature. Deviations from circularity can lead to both over- and underestimation of vortex sizes depending on the vortex orientation. Since isotropy is one of the characteristic properties of turbulent movements one may presume that from a statistical point of view both cases occur equally so that no systematic error is made.~~

As stated in section 3 we found ~~45~~ 25 episodes of turbulence that allowed the derivation of ~~*the vortex radius* L~~ and ~~*circumferential velocity* v_{res}~~. Using equation (1), the energy dissipation rate is then calculated by $\epsilon = \frac{v_{res}^3}{L}$. The resulting ~~eddy diffusion coefficients K~~ values are shown in Figure 5. We assume a general read-out error of ± 3 pixels, which corresponds to a distance of ± 72 m. ~~The circumferential velocity~~Velocities ~~is~~ are determined by reading the distance a ~~patch on the rotating cylinder surface~~feature covers within an episode of at least ten images, which corresponds to a time span of 28 s. Thus, ~~the circumferential velocity~~velocities ~~is~~ are estimated with an error of $\pm 2.6\,\mathrm{m\,s^{-1}}$. The arising uncertainties of ~~$K\epsilon$~~ are calculated following the rules of error propagation.

The values of ~~$K\epsilon$~~ range from 0.0812 to ~~1.94~~9.03 ~~$\cdot 10^4$ $\mathrm{m^{2s^{-1}}}$~~ W kg^{-1}. The ~~mean~~ median value is ~~0.76~~1.45 ~~$\cdot 10^4$ $\mathrm{m^2 s^{-1}}$~~ W kg^{-1}~~(standard deviation of $0.53 \cdot 10^4$ $\mathrm{m^2 s^{-1}}$) and we retrieve a median of $0.59 \cdot 10^4$ $\mathrm{m^2 s^{-1}}$. It is difficult to exactly quantify the error of manual parameter determination from the images. However, in this work we rather focus on the order of magnitude of K. When calculating K two distance values are read from the images (one for the vortex size and one for the determination of the circumferential speed). Considering Eq. (1), a mistake of factor 10 is made for K if these distances are misread by a factor of at least $\sqrt{10}$. The shortest (and therefore most difficult to determine) diameter in our analysed examples was 768 m. For an error of one order of magnitude of K this distance must be misread as either shorter than 243 m or longer than 2428 m, i.e. a distance of 32 pixels must be wrongly interpreted as shorter than 9 pixels or longer than 101 pixels. This lies far beyond the read-out uncertainty of ± 3 pixels we introduced above and can be assumed to be much worse than any read-out error one would normally make.~~

~~The energy dissipation rate ϵ can be estimated from the eddy diffusion coefficient K according to Eq. (2) using the BV frequency as described by Eq. (3).~~

~~As can be seen in Figure 5 the energy dissipation rate of the observed turbulence events is in the range $0.63 - 14.21\,\mathrm{W kg^{-1}}$.~~

Assuming the duration of dissipation being equal to the lifetime of the vortex the energy dissipation rate can be converted into the amount of dissipated energy per mass. This is only done for those vortices that both form and decay within the FOV. The time intervals of dissipation are between ~~146~~241 s and 922 s (~~2.~~4.0 – 15.4 min) and can also be found in Table 1. Events are labelled as 'out of FOV' or as 'clouds' if either the formation or the decay of the vortex cannot be observed. No further analysis is performed for these events.

Multiplying energy dissipation rate and duration of dissipation equals the energy per mass that is released in the turbulent process. We retrieve values between ~~220~~30 and ~~6346~~3015 J kg^{-1}. Given that the released energy is entirely converted into heat we can make a rough estimate of the resulting temperature change by assuming isobaric conditions (may be approximately fulfilled due to the stable stratification of the atmosphere and small vertical dimension of eddies) and dividing energy per mass by the specific heat capacity of dry air (10^3 J K^{-1} kg^{-1}). The resulting temperature changes in this work are in the range 0.03~~2~~ - ~~6.3~~3.02 K. ~~64 % (21 out of 33) of these values are larger than one Kelvin.~~ All values of dissipated energy per mass and maximum temperature change can be found in Table 1.

Since we now have a time series of eddy diffusion coefficients we can compare them to gravity wave activity in the UMLT above OTL. Parallel to FAIM 3, SWIR spectrometers called GRIPS (GRound-based Infrared P-branch Spectrometer) instruments deliver time series of OH* rotational temperatures derived from the OH(3-1) P-branch (1.5 µm-1.6 µm) at an initial temporal resolution of 15 s. Unlike the general instrument details discussed by Schmidt et al. (2013), the GRIPS 9 at OTL has a reduced aperture angle of 6.2 °–FWHM increasing its responsivity to smaller structures. As described in Sedlak et al. (2020), gravity wave activity – the so-called significant wavelet intensity (SWI) – for the periods 6 - 480 min (period resolution 1 min) can be calculated by applying a wavelet analysis to these temperature time series. The FOV of GRIPS 9 is also located above the Gulf of Trieste and in ca. 30 km distance to the FAIM 3 FOV and has a size of approximately 13 km x 19 km. Since the spectroscopic observations are averaged over the entire FOV, GRIPS is most sensitive for gravity waves with horizontal wavelengths of several hundreds of kilometres (Wüst et al., 2016). The time series of nocturnal SWI is restricted to those nights that exhibited at least one of the turbulence episodes presented above and the correlation between the SWI and the eddy diffusion coefficient has been calculated. If there are observations of more than one vortex during one night, the respective eddy diffusion coefficients are averaged to their mean value. The Pearson correlation coefficient and the P value (significance test) are presented in Figure 7. We find ~~a slight but~~almost no significant ~~anti~~correlation for any gravity wave period~~s in the range 122 - 207 min. For these periods the mean value of the correlation coefficient is -0.46. The highest coefficient of anticorrelation is -0.52 at a period of 178 min.~~

5 Discussion

As can be seen in Figure 3, the wave structures we observed exhibit multiple directions. The strong tendency to north-eastern direction in summer and to the (south-)west in winter as observed by Hannawald et al. (2019) for medium-scale gravity waves cannot be confirmed for the waves observed here. However, slight tendencies are apparent in Figure 3. The north-western

component these authors observed during winter at Mt. Sonnblick in Austria with the FOV being positioned north of the Alps also appears in our data during autumn, winter and spring. During summer we find a conspicuous majority of waves propagating into southern direction.

The number of waves propagating eastward and westward is almost equal for the entire data set. However, as stated in section 4.1, more waves are oriented in eastward direction during winter whereas zonal directions are quite balanced during summer. Although the eastward tendency during winter is quite weak, it contradicts the distribution that is expected for gravity waves being created in the lower atmosphere and propagating upward, being subdued to tropospheric and stratospheric wind filtering. The eastward oriented mean wind profile during winter would lead to mainly westward propagating gravity waves reaching the UMLT without encountering critical levels. During summer the stratospheric winds reverse to westward direction, so that eastward oriented gravity waves are filtered in the tropopause and westward oriented gravity waves are filtered in the stratosphere (see, e.g., Hoffmann et al., 2010; Hannawald et al., 2019).

As we have no accompanying wind measurements in the height of our observations it is difficult to decide by means of the period whether the wave structures presented in section 4.1 are small-scale gravity waves or instability features. Ca. 63 % of the wave events have an observed period above the BV period (here we used the climatology presented by Wüst et al., 2020), however these could at least in parts also be Doppler-shifted instability features instead of gravity waves. While the distinction between largely extended wave-fields (bands) and small localized wave structures that are related to instability (ripples) is often made at a horizontal wavelength of 10 - 20 km (Taylor et al., 1997; Nakamura et al., 1999), Li et al. (2017) remark that even structures with horizontal wavelengths of 5 - 10 km may sometimes be gravity waves rather than instability features.

If this would be true for our small-scale wave structures, they might rather be secondary gravity waves (see, e.g., Becker & Vadas, 2018), being generated at greater heights by breaking gravity waves. Secondary gravity waves can either have larger wavelengths and phase speeds than the primary wave if they are created by localized momentum deposition (Vadas & Becker, 2018) or smaller wavelengths and phase speeds if they are induced by the nonlinear flow (wave-mean flow and wave-wave interactions; see, e.g., Bacmeister & Schoeberl, 1989; Franke & Robinson, 1999; Bossert et al., 2017). The former type of secondary gravity waves exhibits a rather broad spectrum of wave parameters with horizontal wavelengths longer than 500 km and horizontal phase speeds between 50 and 250 $m\,s^{-1}$ (Vadas et al., 2018), resulting in periods longer than ca. 30 min. The wave structures found in this work have smaller horizontal wavelengths, phase speeds and periods and could therefore be more likely related to the latter type of secondary waves created by nonlinearities. However, these small-scale secondary waves are unlikely to propagate large vertical distances due to their small horizontal phase speeds (Becker & Vadas, 2018). They have to be generated at even higher altitudes, i.e. close to the mesopause, to be observable with OH* airglow imagers. Hannawald et al. (2019), e.g., deduce from their observations that not only the zonal stratospheric winds but also the meridional circulation in the mesosphere might play a vital role in filtering gravity waves. The meridional mesospheric circulation is oriented southward during summer and northward during winter, being much stronger during summer with ca. 10 - 14 m/s (Yuan et al., 2008). Simulations by Becker & Vadas (2018) show that advection by the background wind determines the direction of a newly created secondary wave. Based on these aspects, the accumulation of southward oriented waves we observe during

summer could be a hint for gravity waves being filtered by the mesospheric circulation and generating subsequent secondary waves with shorter wavelengths and periods, that are provided with a southward phase speed due to advection. This theory is also in good agreement with our observed meridional phase speeds: in the abovementioned velocity range of the summerly meridional mesospheric circulation (10 - 14 m/s) meridional phase speeds are southward in 71 % of cases.

~~The directions of propagation are quite uniformly distributed over all quadrants as can be seen in Figure 2. The strong tendency to north eastern direction in summer and to the (south)west in winter as observed by Hannawald et al. (2019) for medium-scale gravity waves cannot be confirmed for the waves observed here. Only the north western component these authors observed during winter at Mt. Sonnblick in Austria with the FOV being positioned north of the Alps also appears in our data during autumn, winter and spring. During summer we find a conspicuous majority of waves propagating into southern direction.~~

~~The number of waves propagating eastward and westward is almost equal for the entire data set. However, as stated in section 4.1, more waves are oriented in eastward direction during winter (positive zonal phase speed) and in westward direction during summer. Although this tendency is quite weak, it contradicts the distribution that is expected for gravity waves being created in the lower atmosphere and propagating upward, being subdued to stratospheric wind filtering. The eastward oriented mean wind profile during winter would lead to mainly westward propagating gravity waves reaching the UMLT without encountering critical levels. The reversed stratospheric winds during summer would consequently allow some more eastward travelling gravity waves to propagate upward (see e.g. Hoffmann et al., 2010; Hannawald et al., 2019). Since the highest observed phase speed of waves with periods longer than the BV period is only 17.6 $m s^{-1}$, it can be assumed that in the majority we do not observe gravity waves that are originating from low altitudes and are fast enough not to be blocked by the stratospheric wind fields.~~

~~Considering the directional distribution, it is possible that the major part of our waves may be secondary gravity waves (see e.g. Becker & Vadas, 2018), being generated at greater heights by breaking gravity waves. Secondary gravity waves can either have larger wavelengths and phase speeds than the primary wave if they are created by localized momentum deposition (Vadas & Becker, 2018) or smaller wavelengths and phase speeds if they are induced by the nonlinear flow (wave mean flow and wave wave interactions; see e.g. Baemeister & Schoeberl, 1989; Franke & Robinson, 1999; Bossert et al., 2017). The former type of secondary gravity waves exhibits a rather broad spectrum of wave parameters with horizontal wavelengths longer than 500 km and horizontal phase speeds between 50 and 250 $m s^{-1}$ (Vadas et al., 2018), resulting in periods longer than ca. 30 min. The wave structures found in this work have smaller horizontal wavelengths, phase speeds and periods and could therefore be more likely related to the latter type of secondary waves created by nonlinearities. However, these small-scale secondary waves are unlikely to propagate large vertical distances due to their small horizontal phase speeds (Becker & Vadas, 2018). They have to be generated at even higher altitudes, i.e. close to the mesopause, to be observable with OH* airglow imagers. Hannawald et al. (2019) e.g. deduce from their observations that not only the zonal stratospheric winds but also the meridional circulation in the mesosphere might play a vital role in filtering gravity waves. The meridional mesospheric circulation is oriented southward during summer and northward during winter, being much stronger during summer with ca. 10–14 m/s~~

~~(Yuan et al., 2008). Simulations by Becker & Vadas (2018) show that advection by the background wind determines the direction of a newly created secondary wave. Based on these aspects, the accumulation of southward oriented waves we observe during summer could be a hint for gravity waves being filtered by the mesospheric circulation and generating subsequent secondary waves with shorter wavelengths and periods, that are provided with a southward phase speed due to advection. This theory is also in good agreement with our observed meridional phase speeds: in the abovementioned velocity range of the summerly meridional mesospheric circulation (10–14 m/s) meridional phase speeds are southward in 62 % of cases.~~

However, regarding the small horizontal wavelengths below 4.5 km, it is more likely that the major part of the observations presented in section 4.1 are related to instability features. The quite slow phase speeds (mean value 13.3 m/s) are one hint for this as typical gravity wave phase speeds accumulate around 40 m/s (see, e.g., Wachter et al., 2015 and Wüst et al., 2018). If Figure 3b was the phase speed distribution of gravity waves, it is likely that a majority of them would encounter critical levels somewhere and would not be observable in the OH* layer. The small spatial scales of the wave structures we observe are ~~also~~ typical for ripple structures as they were already observed with FAIM 3 (Sedlak et al., 2016). Their short life spans are not excluded by our quality criteria. Tuan et al. (1979) state that oscillations of this type are usually excited at periods of 4 - 10 min, which would explain the large number of wave events we observe in this period range. Observing ripple structures, it would not be surprising to obtain a certain diversity of directions of propagation. In princip~~al~~al, ripples originating from convective instabilities tend to be aligned perpendicular to the wave fronts of the initial wave, whereas ripples arising from dynamic instabilities form parallel to the initial wave fronts (Andreassen et al., 1994; Fritts et al., 1997; Hecht et al., 2000). However, it has been reported that ripples can be rotated by the background wind and that ripples may even be created by a combination of both dynamical and convective instability (Fritts et al., 1996; Hecht, 2004). Considering the fact that the directional peculiarities of our observed wave events fit well with the expected behavior of secondary gravity waves, as discussed above, support the scenario of the wave structures being ripples from dynamic instabilities of secondary gravity waves, that originate from the stratospheric and mesospheric jet. Capturing structures related to instability is not unlikely, considering the numerous observations of turbulent vortices with the FAIM 3 setup.

~~Li et al. (2017) report that ripples are hard to distinguish from small scale gravity waves. Height resolved measurements of the horizontal wind would be needed to determine the local wind shear and make a profound statement about atmospheric instability~~. Nevertheless, height-resolved measurements of the horizontal wind would be needed to determine the local wind shear and make a profound statement about atmospheric instability. ~~capturing structures related to instability is not unlikely, considering the numerous observations of turbulent vortices with the FAIM 3 setup.~~

It has to be kept in mind that a 2d-FFT was used. Thus, periodic structured are assumed to be stationary, i.e., they extend over the entire image. Faint structures that appear only in small parts of the image (as does for example the 550m wave packet in Sedlak et al., 2016; Fig. 2) would be underrepresented by this analysis.

~~There are still very few measurements of turbulent eddy diffusion coefficients in the~~Measuring the eddy diffusion coefficient in the UMLT is still challenging and there are only few studies yet. Rocket measurements ~~of~~ of Lübken (1997) ~~reports *K* to be~~

~~around~~deliver energy dissipation rates between ca. 0.01 and 0.1 $W kg^{-1}$ ~~$10^1 - 10^2$ $m^2 s^{-1}$ at a height of 87 km at~~between 85 and 90 km height at high latitudes. Chau et al. (2020) find an energy dissipation rate of 1.125 $W kg^{-1}$ for their KHI event observed in the summer mesopause and state that this a rather high value compared to the findings of Lübken et al. (2002). Hocking (1999) provides a rescaled overview of earlier values of the energy dissipation rate and these have a maximum magnitude of 0.1 $W kg^{-1}$. Hecht et al. (2021) derive a value of 0.97 $W kg^{-1}$ from airglow images of a KHI event. ~~Hodges (1969) states that the eddy diffusion coefficient caused by gravity waves is typically around 10^3 $m^2 s^{-1}$. According to the CIRA (Committee on Space Research (COSPAR) International Reference Atmosphere) climatology of 1986 (NASA National Space Science Data Center, 2007) global values range between magnitudes of 10^2 and 10^3 $m^2 s^{-1}$. LIDAR measurements above New Mexico, USA deliver values that vary strongly around a magnitude of 10^2 $m^2 s^{-1}$ (Liu, 2009). Smith (2012) notes that the WACCM (Whole Atmosphere Community Climate Model) climatology exhibits rather small values with magnitude 10^1 $m^2 s^{-1}$ and that the huge discrepancies of K estimates cannot be fully explained yet.~~ Ranging from 0.08 up to 9.03 $W kg^{-1}$ the values of energy dissipation rate derived here are higher than reported by other studies. However, the median value of 1.45 $W kg^{-1}$ is not too far away from the values of Chau et al. (2020) and Hecht et al. (2021). ~~The here-presented values of K exhibit a magnitude of $10^3 - 10^4$ $m^2 s^{-1}$, which partly agrees with recent results, although some of our values are higher.~~ The vortices we observe do not necessarily mark the small-scale end of the energy cascade. It could be possible that the energy is cascaded further to a larger number of smaller eddies that are no longer visible to our instrument. Parallel in-situ measurements (e.g., lidar, rockets) could be used to estimate the significance of this effect. Additionally, it has to be kept in mind that – except for the studies of Hecht et al. (2021), whose value is quite similar to the median value of our data – the values compared here arise from different measurement techniques with different horizontal, vertical and temporal resolutions, so that the accessible scales are not necessarily identical due to the observational filter effect. ~~Nevertheless, the agreement of the above mentioned authors on eddy parameters in the UMLT is quite good, considering the fact that energy dissipation rate in the upper troposphere and lower stratosphere varies by a factor of more than five orders of magnitude (Li et al., 2016).~~

The derivation of the ~~vortex~~ turbulence parameters performed here is challenging due to the blurred shape of dynamic signatures in the OH* layer. ~~Circumferential speed and vortex radius~~The length scale and velocity scale of turbulent features have been extracted manually by measuring distances in the images and calculating distances from pixel values. ~~and we~~ We tried to quantify the read-out error by providing a measurement uncertainty and minimize it by repeating the analysis workflow on the same data multiple times. However, using equation (1) velocity dominates the length scale due to its power of 3, so that ϵ strongly depends on a parameter, which is quite difficult to extract from the images. All in all, it seems possible to derive turbulence parameters like the ~~eddy diffusion coefficient and~~ energy dissipation rate from high resolution imager data.

The values of ~~eddy diffusion coefficients~~energy dissipation rate derived here show no significant ~~anti~~correlation with gravity wave activity in the period range ~~122~~6 - ~~207~~480 min. Turbulence thus cannot be related to distinct periods of the gravity wave spectrum with the here-presented data. ~~One may assume that turbulent vortices we observe could be predominantly attributed to breaking gravity waves in this period range. If this was the case, stronger wave breaking would manifest as higher eddy diffusion coefficients and result in a lower activity of gravity waves with periods 122–207 min in the UMLT. However,~~ A

larger data basis of turbulence parameters and especially observations of period-resolved gravity wave activity at altitudes below ~~would~~ will be needed to ~~confirm this assumption~~answer the question if all parts of the gravity wave spectrum drive turbulence generation in the UMLT equally.

Assuming that the turbulently dissipated energy is entirely converted into heat we find temperature changes of 0.03 - 3.02 K~~0.2 - 6.3 K~~ that occur within time spans of ~~2.~~4.0 – 15.4 min. Marsh (2011) report chemical heating rates in the atmosphere to be around 3 – 4 K per day. Given that our analysed episodes are typical representatives of turbulent wave breaking, dynamical heating by gravity wave dissipation would deliver the same effect within few minutes at very localized areas in the UMLT as does chemical heating during an entire day for the whole atmosphere.

6 Summary

We present an analysis of small-scale ~~wave~~ dynamics of instability features and turbulence from OH* imager data acquired between 26 October 2017 and 6 June 2019 at Otlica Observatory, Slovenia. Measurements have been performed with the imager FAIM 3, which has a spatial resolution of ca. 24 m pixel^{-1} and a temporal resolution of 2.8 s.

Wave-like structures in the images are systematically identified by applying a 2d-FFT to nocturnal image sequences during clear sky episodes. All ~~wave~~ events meeting our persistency criteria were used to derive a statistical analysis of wave-like structures with horizontal wavelengths between 48 m and 4.5 km. The small horizontal scales are a strong hint that these are likely instability features of breaking gravity waves like ripples. ~~63 % of the wave events have a period longer than the BV period and may be tentatively considered as gravity waves.~~ We ~~find an isotropic distribution of~~generally find variable directions of propagation, which indicates that these wave-like structures may be mostly created above the stratospheric wind fields. However, a weak seasonal dependency is found: zonal directions of ~~wave~~ propagation are slightly more eastward during winter and westward during summer. We speculate these to be instability features generated by breaking secondary gravity waves ~~in the course of wind filtering~~, receiving their zonal direction through advection by the background wind. We find a stronger tendency of southward propagation during summer, which may point to a vital role of gravity wave filtering and excitation of secondary waves and their subsequent instability features by the meridional mesospheric circulation. ~~It is possible that secondary waves and instability features represent the majority of our observed waves.~~

Furthermore, we observed and presented OH* imager observations of turbulence with high spatio-temporal resolution. We estimated turbulence parameters from 245 episodes of ~~vortex~~ eddy observations. ~~The derived values of eddy diffusion coefficients are in the range around 10^3 – 10^4 $m^2 s^{-1}$ and agree mostly with earlier results from rocket and lidar measurements and simulations. Considering the respective values of the BV frequency as calculated by Wüst et al. (2020)~~Following the approach of Hecht et al. (2021) we ~~retrieve~~ derived the energy dissipation rates for our observed events by reading the turbulent length and velocity scale from the image series. Our values range between 0.08 and 9.03 W kg^{-1}~~,~~ and are higher than earlier rocket measurements. The values presented here would ~~that~~ cause ~~estimated~~ localized heatings ~~by~~ of 0.03 - 3.02 K ~~0.2 - 6.3 K~~ per turbulence event. ~~These have the~~The largest of these reach the same order of magnitude as the daily chemical heating rates

as reported by Marsh (2011). Given that the observed events are representative of typical processes of gravity wave dissipation, this emphasizes the importance of carefully integrating gravity wave turbulence into climate simulations.

Being able to derive reasonable values of UMLT turbulence parameters from imager data represents an important progress for measurement techniques of atmospheric dynamics. Airglow imagers are much cheaper and more flexible than rockets or lidars. Considering the huge amount of data, artificial intelligence could be used in the future to identify and analyse turbulent episodes.

Appendix A

Derivation of the eddy diffusion coefficient K (Eq. (1))

The derivation of the eddy diffusion coefficient shown here is based on Prölss (2001). It is assumed that a cylindrical vortex with radius r_e and cylinder height d is excited in the course of turbulence, which rotates around an axis perpendicular to the circular cylinder bases (Figure 8). We consider an atmosphere of particle number density n (varying with height z) in which a side gas i with particle number density n_i exhibits a concentration gradient $\frac{d\left(\frac{n_i}{n}\right)}{dz}$ (concentration as ratio of particle numbers of side gas and total atmosphere) perpendicular to the rotational axis. Maximum mixing results when the cylinder rotates half a turn, i.e. when the cylinder segment of high concentration and the cylinder segment of low concentration switch places. This induces a net particle flux through the center plane A of the cylinder.

Let us consider two cylinder segments 1 and 2 of thickness ds, width $2b$ and depth d at distance $\pm s$ from the center plane, thus having the volume $dV = d\ 2b\ ds$. The number of side gas particles they contain is

$$(dN_i)_1 = dV\ n_1 \left(\frac{n_i}{n}\right)_1 \quad (4)$$

and

$$(dN_i)_2 = dV\ n_2 \left(\frac{n_i}{n}\right)_2 = dV\ n_2 \left[\left(\frac{n_i}{n}\right)_1 + \frac{d\left(\frac{n_i}{n}\right)}{dz} 2s + \cdots\right]. \quad (5)$$

During half a vortex rotation the segments 1 and 2 move towards the center plane. n and n_i change with height while $\frac{n_i}{n}$ remains constant ($n(z) = n$ at the center plane). This results in a net exchange of

$$(dN_i)_A = [(dN_i)_1 - (dN_i)_2]_A \approx -dV\ n \frac{d\left(\frac{n_i}{n}\right)}{dz} 2s \quad (6)$$

side gas particles through the center plane $A = 2\ r_e\ d$ (i.e. we subtracted Eq. (5) from Eq. (4)). With a circumferential velocity v_e and an exchange time of $\Delta t = \frac{\pi r_e}{v_e}$ for half a rotation this leads to a differential particle flux density of

$$d\Phi_e = \frac{(dN_i)_A}{A\ \Delta t} = -dV\ n \frac{d\left(\frac{n_i}{n}\right)}{dz} 2s \frac{1}{A\ \Delta t} = -d\ 2b\ ds\ n \frac{d\left(\frac{n_i}{n}\right)}{dz} 2s \frac{1}{2\ r_e\ d} \frac{v_e}{\pi r_e} = -2\sqrt{r_e^2 - s^2}\ ds\ n \frac{d\left(\frac{n_i}{n}\right)}{dz} s \frac{1}{r_e} \frac{v_e}{\pi r_e}. \quad (7)$$

Please note that b has been replaced by $\sqrt{r_e^2 - s^2}$ according to the Pythagoras Theorem.

~~Integration over all cylinder segments yields the total flux density~~

$$\Phi_e = \int_{s=0}^{r_e} d\Phi_e = -\frac{2}{\pi}\frac{v_e}{r_e^2} n \frac{d\left(\frac{n_i}{n}\right)}{dz} \int_{s=0}^{r_e} \sqrt{r_e^2 - s^2}\, s\, ds\,. \quad (8)$$

~~The integral can be solved by substituting $x := r_e^2 - s^2$ and therefore $\frac{dx}{ds} = -2s$.~~

~~Then~~

$$\int_{s=0}^{r_e} \sqrt{r_e^2 - s^2}\, s\, ds = -\frac{1}{2}\int_{r_e^2}^{0} \sqrt{x}\, dx = -\frac{1}{3}\left[x^{\frac{3}{2}}\right]_{r_e^2}^{0} = \frac{1}{3} r_e^3 \quad (9)$$

~~so that~~

$$\Phi_e = -\frac{2}{3\pi} r_e\, v_e\, n \frac{d\left(\frac{n_i}{n}\right)}{dz}. \quad (10)$$

~~Analogously to Fick's law of molecular diffusion we can write the flux density of eddy diffusion as~~

$$\Phi_e = -K\, n \frac{d\left(\frac{n_i}{n}\right)}{dz} \quad (11)$$

~~where~~

$$K = \frac{2}{3\pi} r_e v_e$$

~~is the eddy diffusion coefficient.~~

Data availability

The data are archived at the WDC-RSAT (World Data Center for Remote Sensing of the Atmosphere). The FAIM and GRIPS instruments are part of the Network for the Detection of Mesospheric Change, NDMC (https://ndmc.dlr.de).

Author contribution

The conceptualisation of the project, the funding acquisition as well as the administration and supervision were done by MB and SW. The operability of the instrument was assured by RS. SS provided us the opportunity to set up our instrument at Otlica Observatory and took care of the maintenance. The algorithm for retrieving wave statistics was written by PH. The analyses of wave statistics and turbulence from FAIM 3 images as well as the visualization of the results were performed by RS. Setup, operation and data reduction for GRIPS 9 was done by CS. The interpretation of the results benefited from fruitful discussions between PH, CS, SW, MB, and RS. The original draft of the manuscript was written by RS. Careful review of the draft was performed by all co-authors.

Competing interests

The authors declare that they have no conflict of interest.

Acknowledgement

This research received funding from the Bavarian State Ministry of the Environment and Consumer Protection by grant number TKP01KPB-70581 (Project VoCaS-ALP).

References

Adams, G. W., Peterson, A. W., Brosnahan, J. W., and Neuschaefer, J. W.: Radar and optical observations of mesospheric wave activity during the lunar eclipse of 6 July 1982, J. Atmos. Terr. Phys., 50, 11–20, 1988.

Andreassen, Ø., Wasberg, C. E., Fritts, D. C., and Isler, J. R.: Gravity wave breaking in two and three dimensions 1. Model description and comparison of two-dimensional evolutions, J. Geophys. Res., 99, 8095–8108, 1994.

Bacmeister, J. T., & Schoeberl, M. R.: Breakdown of vertically propagating two-dimensional gravity waves forced by orography, J. Atmos. Sci., 46, pp. 2109–2134., 1989.

Baker, D. J. and Stair, A. T.: Rocket Measurements of the Altitude Distributions of the Hydroxyl Airglow, Phys. Scripta, 37, 611–622, https://doi.org/10.1088/0031-8949/37/4/021, 1988.

Baumgarten, G. and Fritts, D. C.: Quantifying Kelvin-Helmholtz instability dynamics observed in noctilucent clouds: 1. Methods and observations, J. Geophys. Res. Atmos., 119, pp. 9324-9337, doi:10.1002/2014JD021832, 2014.

Becker, E. and Vadas, S. L.: Secondary Gravity Waves in the Winter Mesosphere: Results From a High-Resolution Global Circulation Model, J. Geophys. Res.: Atmospheres, 123, pp. 2605–2627, https://doi.org/10.1002/2017JD027460, 2018.

Beldon, C. L., and Mitchell, N. J.: Gravity waves in the mesopause region observed by meteor radar, 2: Climatologies of gravity waves in the Antarctic and Arctic, J. Atmos. Sol.-Terr. Phy., 71, pp. 875-884, https://doi.org/10.1016/j.jastp.2009.03.009, 2009.

Bittner, M., Offermann, D., and Graef, H. H.: Mesopause temperature variability above a midlatitude station in Europe, J. Geophys. Res., Vol. 105, pp. 2045-2058, 2000.

Bossert, K., Kruse, C. G., Heale, C. J., Fritts, D. C., Williams, B. P., Snively, J. B., Pautet, P.-D., and Taylor, M. J.: . Secondary gravity wave generation over New Zealand during the DEEPWAVE campaign. Journal of Geophysical Research: Atmospheres, 122, pp. 7834–7850, https://doi.org/10.1002/2016JD026079, 2017.

Browning, K. A.: Structure of the atmosphere in the vicinity of large-amplitude Kelvin–Helmholtz billows, Q. J. Roy. Meteor. Soc., 97, 283–299, 1971.

Chau, J. L., Urco, J. M., Avsarkisov, V., Vierinen, J. P., Latteck, R., Hall, C. M., and Tsutsumi, M.: Four-Dimensional Quantification of Kelvin-Helmholtz Instabilities in the Polar Summer Mesosphere Using Volumetric Radar Imaging, Geophys. Res. Let., 47, e2019GL086081, https://doi.org/10.1029/2019GL086081, 2020.

de la Cámara, A., Lott, F., and Abalos, M.: Climatology of the middle atmosphere in LMDz: Impact of source-related parameterizations of gravity wave drag, J. Adv. Model. Earth Syst., 8, 1507-1525, doi:10.1002/2016MS000753, 2016.

Espy, P. J., and Stegman, J.: Trends and variability of mesospheric temperature at high-latitudes, Phys. Chem. Earth, 27, pp. 543-553, 2002.

Espy, P. J., Hibbins, R. E., Jones, G. O. L., Riggin, D. M., and Fritts, D. C.: Rapid, large-scale temperature changes in the polar mesosphere and their relationship to meridional flows, Geophys. Res. Letters, Vol. 30, No. 5, 1240, doi:10.1029/2002GL016452, 2003.

Franke, P. M. and Robinson, W. A.: Nonlinear behaviour in the propagation of atmospheric gravity waves, J. Atmos. Sci., 56, pp. 3010-3027, 1999.

French, W. J. R., and Burns, G. B.: The influence of large-scale oscillations on long-term trend assessment in hydroxyl temperatures over Davis, Antarctica, J. Atmos. Sol.-Terr. Phys., 66, pp. 493-506, doi:10.1016/j.jastp.2004.01.027, 2004.

Fritts, D. C. and Alexander, M. J.: Gravity wave dynamics and effects in the middle atmosphere, Review of Geophysics, 41, 1, doi:10.1029/2001RG000106, 2003.

Fritts, D. C., Garten, J. F., and Andreassen, Ø.: Wave breaking and transition to turbulence in stratified shear flows, J. Atmos. Sci., 53, 1057–1085, 1996.

Fritts, D. C., J. R. Isler, J. H. Hecht, R. L. Walterscheid, and O. Andreassen: Wave breaking signatures in sodium densities and OH nightglow. 2. Simulation of wave and instability structures, J. Geophys. Res., 102, 6669–6684, doi:10.1029/96JD01902, 1997.

Gardner, C. S., Zhao, Y., and Liu, A. Z.: Atmospheric stability and gravity wave dissipation in the mesopause region, J. Atmos. Sol.-Terr. Phy., 64, 923–929, 2002.

Gargett, A. E.: Velcro Measurement of Turbulence Kinetic Energy Dissipation Rate ϵ, Journal of Atmospheric and Oceanic Technology, 16, pp. 1973-1993, 1999.

Hannawald P., Schmidt, C., Wüst , S., and Bittner, M.: A fast SWIR imager for observations of transient features in OH airglow, Atmos. Meas. Tech., 9 1461-1472, doi:10.5194/amt-9-1461-2016, 2016.

Hannawald, P., Schmidt, C., Sedlak, R., Wüst, S., and Bittner, M.: Seasonal and intra-diurnal variability of small-scale gravity waves in OH airglow at two Alpine stations, Atmos. Meas. Tech., 12,457–469, DOI: 10.5194/amt-12-457-2019, 2019.

Hecht, J. H., Walterscheid, R. L., Fritts, D. C., Isler, J. R., Senft, D. C., Gardner, C. S., and Franke, S. J.: Wave breaking signatures in OH airglow and sodium densities and temperatures 1. Airglow imaging, Na lidar, and MF radar observations, J. Geophys. Res., Vol. 102, No. D6, pp. 6655-6668, 1997.

Hecht, J. H., C. Fricke-Begemann, R. L. Walterscheid, and J. Höffner: Observations of the breakdown of an atmospheric gravity wave near the cold summer mesopause at 54N, Geophys. Res. Lett., 27, 879–882, doi:10.1029/1999GL010792, 2000.

Hecht, J. H.: Instability layers and airglow imaging, Review of Geophysics, Vol. 42, 2004.

Hecht, J. H., Wan, K., Gelinas, L. J., Fritts, D. C., Walterscheid, R. L., Rudy, R. J., Liu, A. Z., Franke, S. J., Vargas, F. A., Pautet, P. D., Taylor, M. J., and Swenson, G. R.: The life cycle of instability features measured from the Andes Lidar Observatory over Cerro Pachon on 24 March 2012, J. Geophys. Res. Atmos., 119, 8872–8898, 2014.

Hecht, J. H., Fritts, D. C., Gelinas, L. J., Rudy, R. J., Walterscheid, R. L., and Liu, A. Z.: Kelvin-Helmholtz Billow Interactions and Instabilities in the Mesosphere Over the Andes Lidar Observatory: 1. Observations, JGR Atmospheres, 126, e2020JD033414. https://doi.org/10.1029/2020JD033414, 2021.

Hines, C.O. and Tarasick, D.W.: On the detection and utilization of gravity waves in airglow studies, Planet. Space Sci., 35, 851–866, https://doi.org/10.1016/0032-0633(87)90063-8, 1987.

Hocking, W. K.: Measurement of turbulent energy dissipation rates in the middle atmosphere by radar techniques: A review, Radio Sci., 20, 6, pp. 1403-1422, 1985.

Hocking, W. K.: The dynamical parameters of turbulence theory as they apply to middle atmosphere studies, Earth Planets Space, 51, pp. 525-541, 1999.

~~Hodges, R. R.: Eddy diffusion coefficients due to instabilities in internal gravity waves, J. Geophys. Res., 74, Issue 16, pp. 4087-4090, 1969.~~

Hoffmann P., Becker, E., Singer, W., and Placke, M.: Seasonal variation of mesospheric waves at northern middle and high latitudes, J. Atmos. Sol.-Terr. Phy., 72, pp. 1068-1079, 2010.

Holton, J. R.: The influence of gravity wave breaking on the general circulation of the middle atmosphere, J. Atmos. Sci., 40, pp. 2497-2507, 1983.

Holton, J. R. and Alexander, M. J.: Gravity waves in the mesosphere generated by tropospheric convection, Tellus, 51A-B, pp. 45-58, 1999.

Li, Z., Liu, A. Z., Lu, X., Swenson, G. R., and Franke, S. J.: Gravity wave characteristics from OH airglow imager over Maui, J. Geophys. Res., Vol. 116, Issue D22, 2011.

~~Li, Q., Rapp, M., Schrön, A., Schneider, A., and Stober, G.: Derivation of turbulent energy dissipation rate with the Middle Atmosphere Alomar Radar System (MAARSY) and radiosondes at Andøya, Norway, Ann. Geophys., 34, pp. 1209-1229, doi:10.5194/angeo-34-1209-2016, 2016.~~

Li, J., Li, T., Dou, X., Fang, X., Cao, B., She, C.-Y., Nakamura, T., Manson, A., Meek, C., and Thorsen, D.: Characteristics of ripple structures revealed in OH airglow images, J. Geophys. Res. Space Physics, 122, pp. 3748-3759, doi:10.1002/2016JA023538, 2017.

Lindzen, R. S.: Turbulence and stress owing to gravity wave and tidal breakdown, J. Geophys. Res.: Oceans banner, 86, C10, pp. 9707-9714, 1981.

~~Liu, A. Z.: Estimate eddy diffusion coefficients from gravity wave vertical momentum and heat fluxes, Geophys. Res. Let., Vol. 36, L08806, doi:10.1029/2009GL037495, 2009.~~

Liu, G. and Shepherd, G. G.: An empirical model for the altitude of the OH nightglow emission, Geophys. Res. Let., Vol. 33, L09805, doi:10.1029/2005GL025297, 2006.

Lübken, F.-J., von Zahn, U., Thrane, E. V., Blix, T., Kokin, G. A., and Pachomov, S. V.: In situ measurements of turbulent energy dissipation rates and eddy diffusion coefficients during MAP/WINE, J. Atmos. Terr. Phys., Vol. 49, Nos. 7/8, pp. 763-775, 1987.

Lübken, F.-J.: Seasonal variation of turbulent energy dissipation rates at high latitudes as determined by in situ measurements of neutral density fluctuations, J. Geophys. Res., Vol. 102, No. D12, pp. 13441-13456, 1997.

Lübken, F.-J., Rapp, M. and Hofmann, P.: Neutral air turbulence and temperatures in the vicinity of polar mesospheric summer echoes, J. Geophys. Res., 107, D15, https://doi.org/10.1029/2001JD000915, 2002.

Marsh, D. R.: Chemical-Dynamical Coupling in the Mesosphere and Lower Thermosphere, Aeronomy of the Earth's Atmosphere and Ionosphere (eds. Abdu, M. A. and Pancheva, D., Coed. Bhattacharyya, A.), IAGA Special Sopron Book Series 2, doi:10.1007/978-94-007-0326-1_1, Springer Science+Business Media B. V., 2011.

Moreels, G., Clairemidi, J., Faivre, M., Mougin-Sisini, D., Kouahla, M. N., Meriwether, J. W., Lehmacher, G. A., Vidal, E., and Veliz, O.: Stereoscopic imaging of the hydroxyl emissive layer at low latitudes, Planet. Space Sci., 56, pp. 1467-1479, 2008.

Mulligan, F.J., Horgan, D.F., Galligan, J.G., Griffin, E.M.: Mesopause temperatures and integrated band brightnesses calculated from airglow OH emissions recorded at Maynooth (53.21N, 6.41W) during 1993. Journal of Atmospheric and Terrestrial Physics 57 (13), 1623–1637, 1995.

Nakamura, T., Higashikawa, A., Tsuda, T., and Matsuhita, Y.: Seasonal variations of gravity wave structures in OH airglow with a CCD imager at Shigaraki, Earth Planets Space, 51, 897-906, 1999.Offermann, D., Gusev, O., Donner, M., Forbes, J. M., Hagan, M., Mlynczak, M. G., Oberheide, J., Preusse, P., Schmidt, H., and Russell III, J. M.: Relative intensities of middle atmosphere waves, J. Geophys. Res., 114, D06110, doi:10.1029/2008JD010662, 2009.

~~NASA National Space Science Data Center: COSPAR International Reference Atmosphere (CIRA-86): Global compilations of ground based, radiosonde, NIMBUS satellite and MSIS-86 model data from 1963-1973, NCAS British Atmospheric Data Centre, available at: https://catalogue.ceda.ac.uk/uuid/d758b820b4eba646ff0d6e05b552e23d (last access: 22 September 2020), 2007.~~

Offermann, D., Gusev, O., Donner, M., Forbes, J. M., Hagan, M., Mlynczak, M. G., Oberheide, J., Preusse, P., Schmidt, H., and Russel III, J. M.: Relative intensities of middle atmosphere waves, J. Geophys. Res., Vol. 114, D06110, doi:10.1029/2008JD010662, 2009.

Pautet, P. D., Taylor, M. J., Pendleton, W. R., Zhao, Y., Yuan, T., Esplin, R., & McLain, D.: Advanced mesospheric temperature mapper for high-latitude airglow studies, Appl. Opt., 53(26), 5934-5943, 2014.

Peterson, A. W.: Airglow events visible to the naked eye, Appl. Optics, 18, 3390–3393, doi:10.1364/AO.18.003390, 1979.

Peterson, A. W. and Kieffaber, L. M.: Infrared Photography of OH Airglow Structures, Nature, Vol. 242, pp. 321-322, 1973.

~~Prölss, G.: Physik des erdnahen Weltraums: Eine Einführung. Springer Verlag, Ausgabe 2, ISBN 3642188079, 9783642188077, 2001.~~

Reisin, E.R., and Scheer, J.: Vertical propagation of gravity waves determined from zenith observations of airglow. Adv. Space Res., Vol. 27, 1743–1748, 2001.

Satomura, T. and Sato, K.: Secondary generation of gravity waves associated with the breaking of mountain waves, J. Atmos. Sci., 56, pp. 3847-3858, 1999.

Schmidt, C., Höppner, K., and Bittner, M.: A ground-based spectrometer equipped with an InGaAs array for routine observations of OH(3-1) rotational temperatures in the mesopause region, J. Atmos. Sol.-Terr. Phy., 102, pp. 125-139, 2013.

Schmidt, C., Dunker, T., Lichtenstern, S., Scheer, J., Wüst, S., Hoppe, U.-P., and Bittner, M.: Derivation of vertical wavelengths of gravity waves in the MLT-region from multispectral airglow observations, J. Atmos. Sol.-Terr. Phy., 173, pp. 119-127, 2018.

Sedlak, R., Hannawald, P., Schmidt, C., Wüst, S., and Bittner, M.: High-resolution observations of small-scale gravity waves and turbulence features in the OH airglow layer, Atmos. Meas. Tech., 9, pp. 5955-5963, doi: 10.5194/amt-9-5955-2016, 2016.

Sedlak, R., Zuhr, A., Schmidt, C., Wüst, S., Bittner, M., Didebulidze, G. G., and Price, C.: Intra-annual variations of spectrally resolved gravity wave activity in the UMLT region, Atmos. Meas. Tech., 13, pp. 5117-5128, https://doi.org/10.5194/amt-2020-13-5117-2020, 2020.

Silber, I., Price, C., Schmidt, C., Wüst, S., Bittner, M., and Pecora, E.: First ground-based observations of mesopause temperatures above the Eastern-Mediterranean Part I: multi-day oscillations and tides, J. Atmos. Sol.-Terr. Phys., 155, 95-103, 2017.

Smith, S., Baumgardner, J., and Mendillo, M.: Evidence of mesospheric gravity-waves generated by orographic forcing in the troposphere, Geophys. Res. Lett., Vol. 36, 2009.

Taylor, M. J.: A review of advances in imaging techniques for measuring short period gravity waves in the mesosphere and lower thermosphere, Adv. Space Res., 19, pp. 667-676, 1997.

Taylor, M. J. and Hapgood, M. A.: On the origin of ripple-type wave structure in the OH nightglow emission, Planet. Space Sci., 38, 1421–1430, 1990.

Tuan, T. F., Hedinger, R., Silverman, S. M., and Okuda, M.: On gravity wave induced Brunt-Vaisala oscillations, J. Geophys. Res.: Space Phys., Vol. 84, A2, pp. 393-398, 1979.

Vadas, S. L. and Fritts, D. C.: Gravity wave radiation and mean responses to local body forces in the atmosphere, J. Atmos. Sci., Vol. 58, Issue 16, pp. 2249-2279, doi:10.1175/1520-0469(2001)058, 2001.

Vadas, S.L., J. Zhao, X. Chu and E. Becker: The Excitation of secondary gravity waves from local body forces: Theory and observation, J. Geophys. Res. Atmospheres, 123, https://doi.org/10.1029/2017JD027970, 2018.

Vadas, S. L. and Becker, E.: Numerical Modeling of the Excitation, Propagation, and Dissipation of Primary and Secondary Gravity Waves during Wintertime at McMurdo Station in the Antarctic, J. Geophys. Res.: Atmospheres, 123, pp. 9326-9369, 2018.

Wachter, P., Schmidt, C., Wüst, S., and Bittner, M.: Spatial gravity wave characteristics obtained from multiple OH(3-1) airglow temperature time series, J. Atmos. Sol.-Terr. Phy., 135, pp. 192-201, 2015.

~~Weinstock, J.: Vertical Turbulent Diffusion in a Stably Stratified Fluid, J. Atmos. Sci., Vol. 35, pp. 1022–1027, 1978.~~

Wüst, S., Wendt, V., Schmidt, C., Lichtenstern, S., Bittner, M., Yee, J.-H., Mlynczak, M. G., and Russell III, J. M.: Derivation of gravity wave potential energy density from NDMC measurements, J. Atmos. Sol.-Terr. Phys., 138, 32–46, https://doi.org/10.1016/j.jastp.2015.12.003, 2016.

Wüst, S., Schmidt, C., Bittner, M., Silber, I., Price, C., Yee, J.-H., Mlynczak, M. G., and Russel III, J. M.: First ground-based observations of mesopause temperatures above the Eastern-Mediterranean Part II: OH*-climatology and gravity wave activity, J. Atmos. Sol.-Terr. Phys., 155, 104-111, 2017a.

Wüst, S., Bittner, M., Yee, J.-H., Mlynczak, M. G., and Russell III, J. M.: Variability of the Brunt–Väisälä frequency at the OH* layer height, Atmos. Meas. Tech., 10, 4895–4903, https://doi.org/10.5194/amt-10-4895-2017, 2017b.

Wüst, S., Offenwanger, T., Schmidt, C., Bittner, M., Jacobi, C., Stober, G., Yee, J.-H., Mlynczak, M. G., and Russell III, J. M.: Derivation of gravity wave intrinsic parameters and vertical wavelength using a single scanning OH(3-1) airglow spectrometer, Atmos. Meas. Tech., 11, 2937–2947, https://doi.org/10.5194/amt-11-2937-2018, 2018.

Wüst, S., Schmidt, C., Hannawald, P., Bittner, M., Mlynczak, M. G., Russell III, J. M.: Observations of OH-airglow from ground, aircraft, and satellite: investigation of wave-like structures before a minor stratospheric warming. Atmos. Phys. Chem., 19, 6401–6418, DOI: 10.5194/acp-19-6401-2019, 2019.

Wüst, S., Bittner, M., Yee, J.-H., Mlynczak, M. G., and Russell III, J. M.: Variability of the Brunt–Väisälä frequency at the OH∗-airglow layer height at low and midlatitudes, Atmos. Meas. Tech., 13, 6067–6093, https://doi.org/10.5194/amt-13-6067-2020, 2020.

Yuan, T., She, C.-Y., Krueger, D. A., Sassi, F., Garcia, R., Roble, R. G., Liu, H.-L., and Schmidt, H.: Climatology of mesopause region temperature, zonal wind, and meridional wind over Fort Collins, Colorado (41◦ N, 105◦ W), and comparison with model simulations, J. Geophys. Res., 113, D03105, https://doi.org/10.1029/2007JD008697, 2008.

Figures

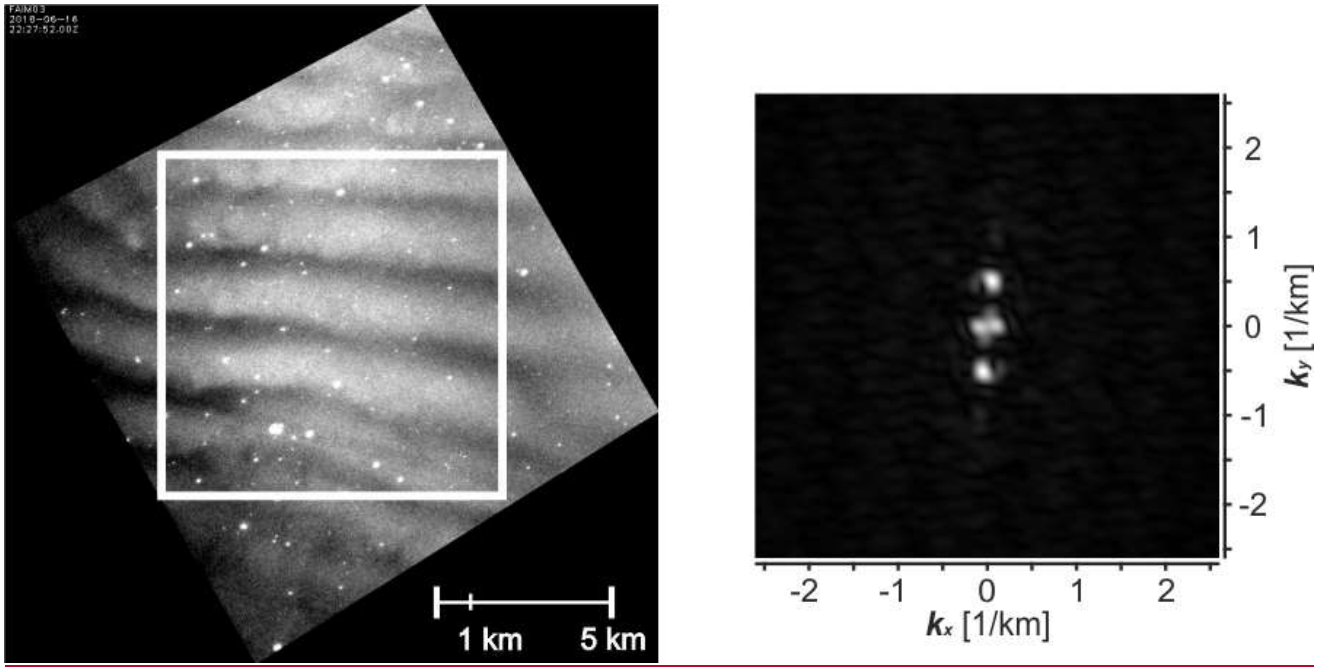

Figure 1. Event from 16 June 2018 22:27:52 UTC. The structure has a horizontal 'wavelength' of ca. 1.9km and extends over the entire image (left). The white square marks the area which is analysed with the 2d-FFT. The respective 2-dimensional spectrum is shown on the right-hand side in the k-space.

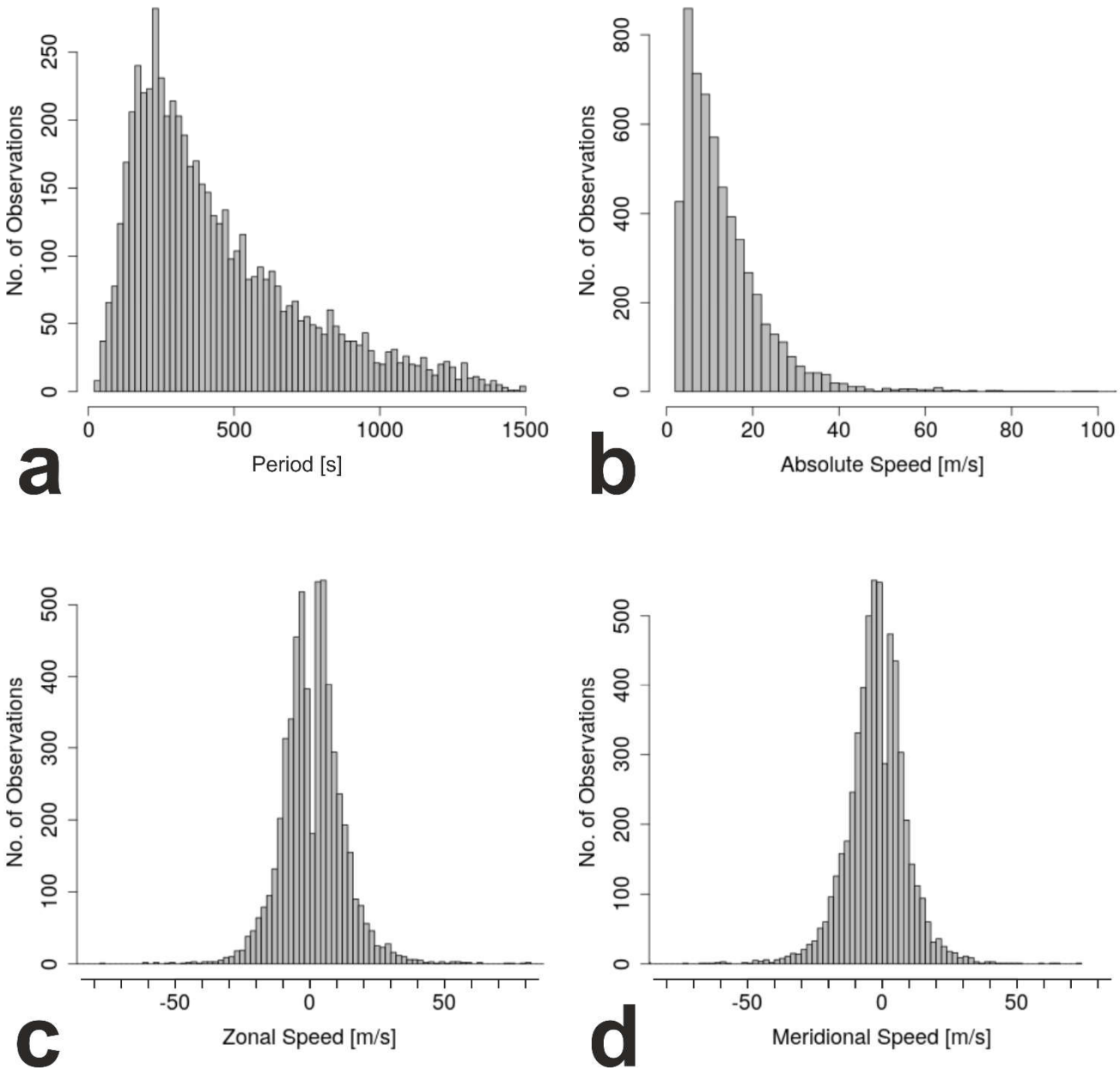

Figure 21. Statistical distribution of observed parameters for wave events with horizontal wavelengths between 48 m and 4.5 km from 26 October 2017 to 6 June 2019 at Otlica, Slovenia. ~~The contribution of wave events with a period longer than the respective BV period is coloured in grey.~~ a) Period. b) Absolute horizontal phase speed. c) Zonal phase speed. d) Meridional phase speed.

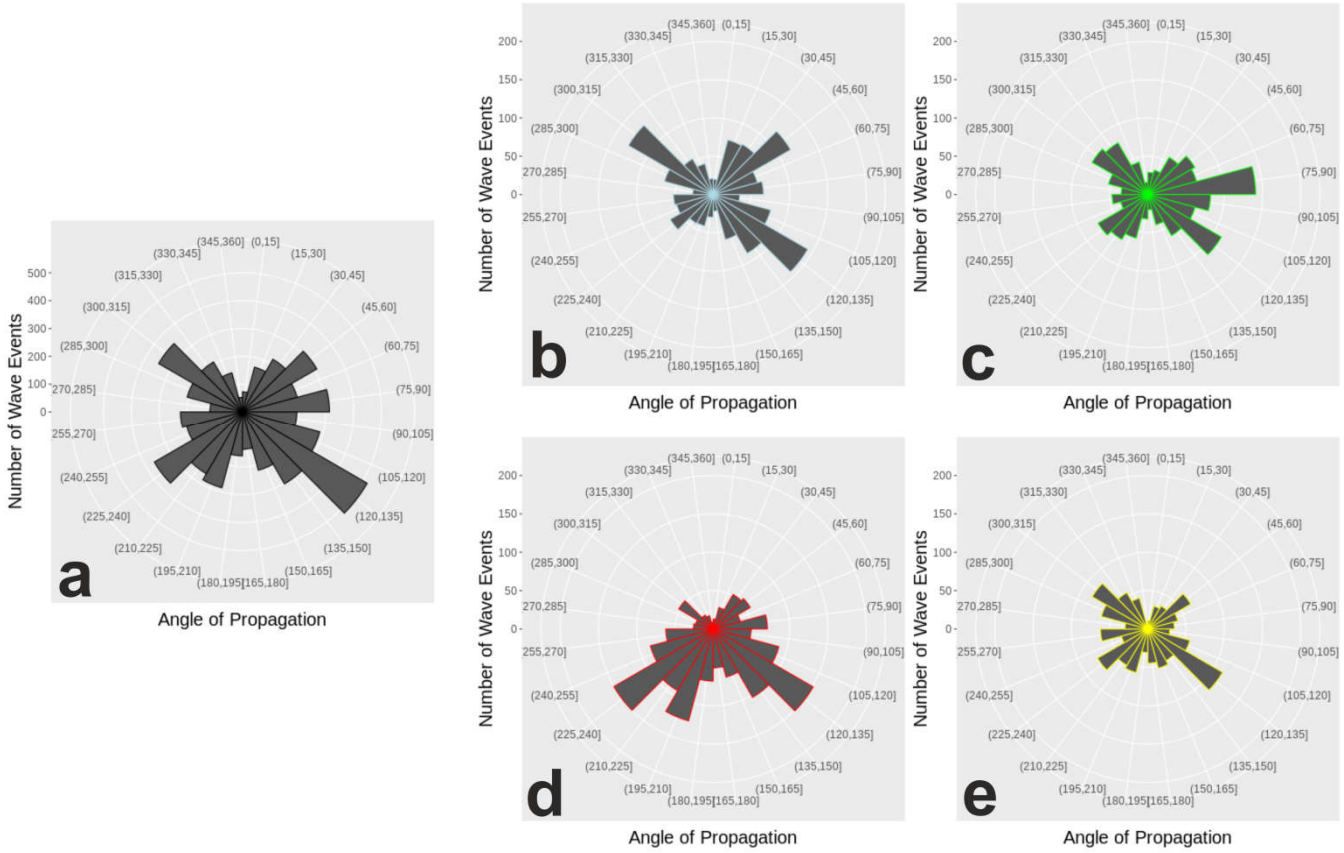

705

Figure 3~~2~~. Statistical distribution of observed directions of propagation for wave events with horizontal wavelengths between 48 m and 4.5 km from 26 October 2017 to 6 June 2019 at Otlica, Slovenia. a) All. b) Winter (Dec-Jan-Feb). c) Spring (Mar-Apr-May). d) Summer (Jun-Jul-Aug). e) Autumn (Sep-Oct-Nov).

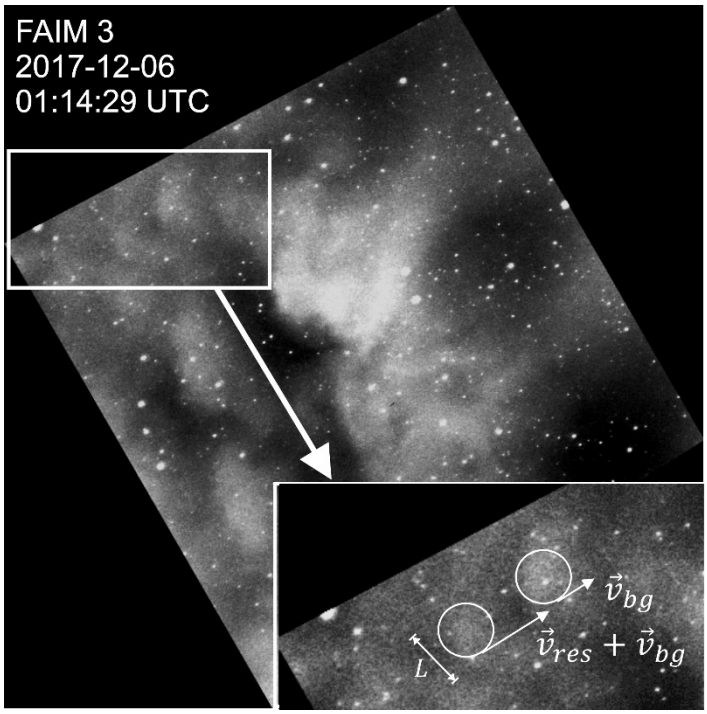

Figure 43. (a) Snapshot (1901:3614:41 29 UTC) of the turbulence episode from 64 November December2018 between 19:32:24 and 19:40:59 UTC. Two patches move in the same directions but have different speeds and are approaching each other. While the feature on the right-hand side seems to be advected by the wind (as do the structures in the entire image) the feature on the left-hand side moves even faster and belongs to those structures that creates the impression of turbulent dynamics. The latter patch moves with the residual velocity that is used in equation (1) plus the background velocity. The length scale L used in equation (1) is given by the size of this feature. he rotational axis (black line) and movement (red arrows) of a vortex are marked in the picture and on a cylinder (b) to guide the eye. This rotation of the vortex is more apparentturbulent episode is attached as in the video supplement to this article (Video 1)video 2 in the supplement of this article.

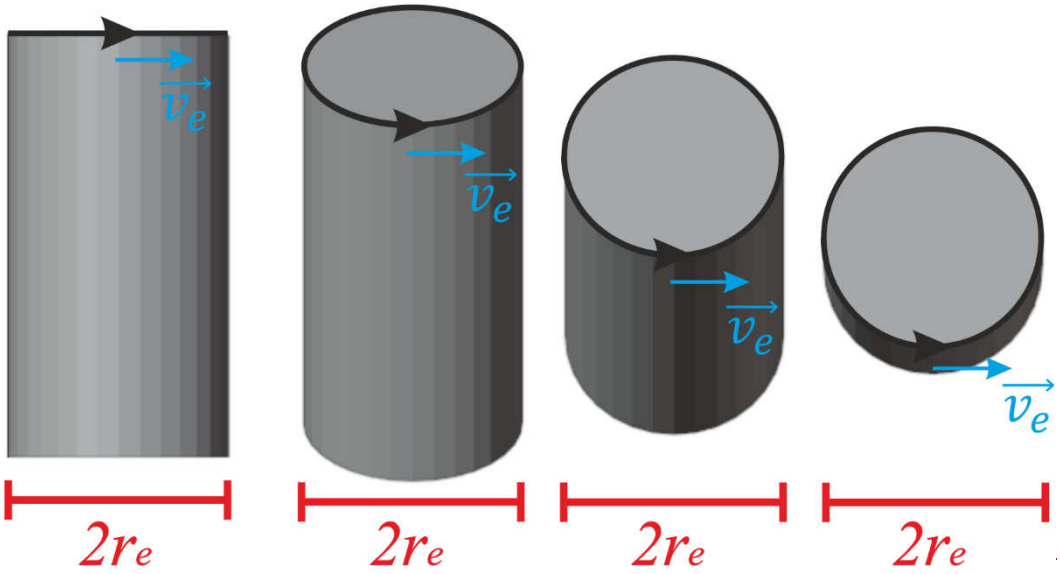

~~Figure 4. Schematic view of a rotating cylinder from different angles. In a 2-dimensional projection, the quantities we read from the images – the vortex radius r_e and the circumferential velocity $\vec{v_e}$ – remain the same for different perspectives.~~

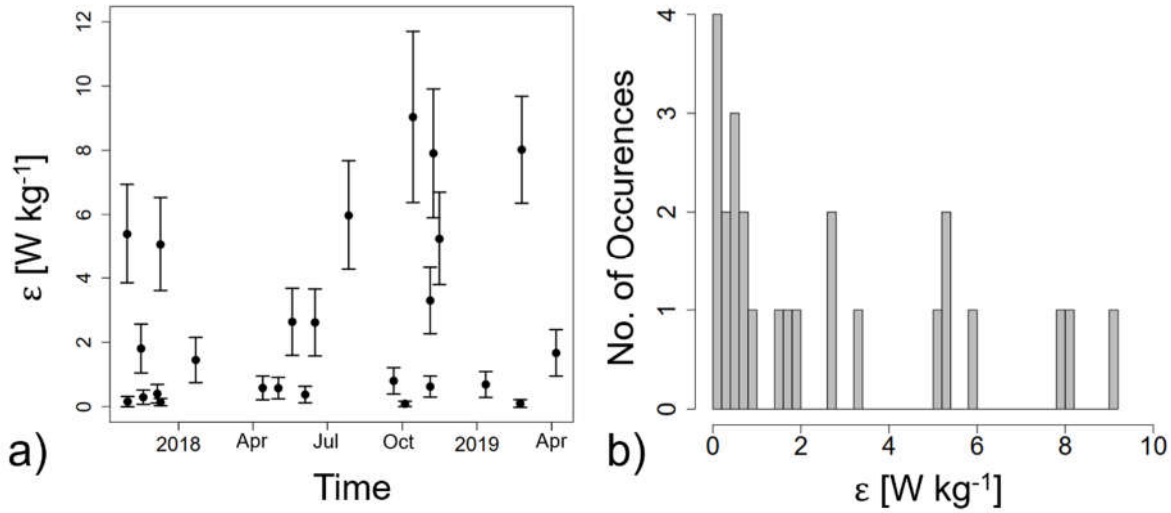

Figure ~~5~~5. a) Temporal evolution of ~~eddy diffusion coefficients~~energy dissipation ~~(black) and energy dissipation rates (grey)~~ of observed turbulence events at OTL (see Table 1). b) Histograms~~s~~ of ~~K and~~ ε.

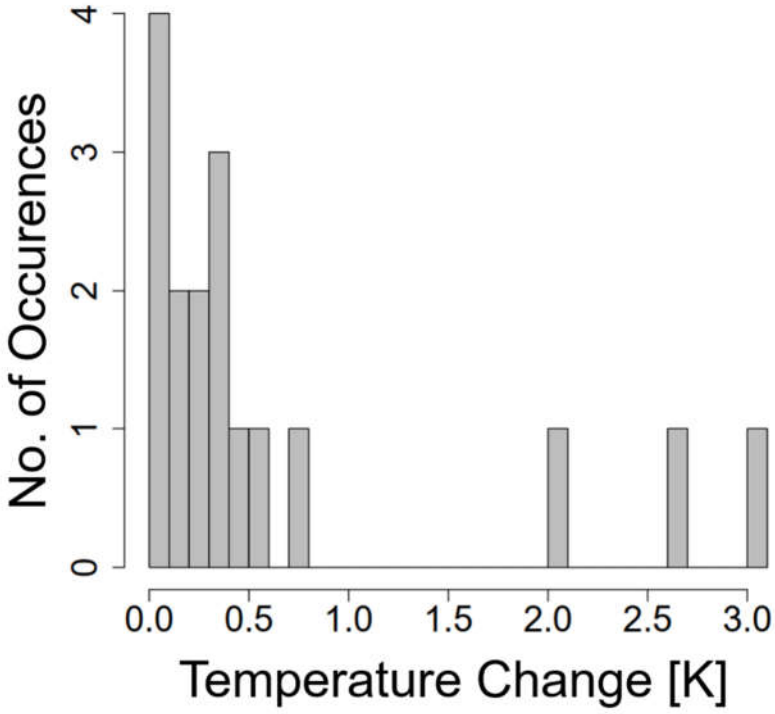

Figure ~~6. a) Temporal evolution of dissipated energy per mass [J/kg] and respective temperature change [K] of observed turbulence events at OTL (see Table 1), assuming isobaric conditions and complete conversion of dissipated energy into heat. b)~~ Histogram of ~~dissipated energy per mass and~~ temperature change resulting from the observed turbulence events assuming isobaric heating and full conversion into heat.

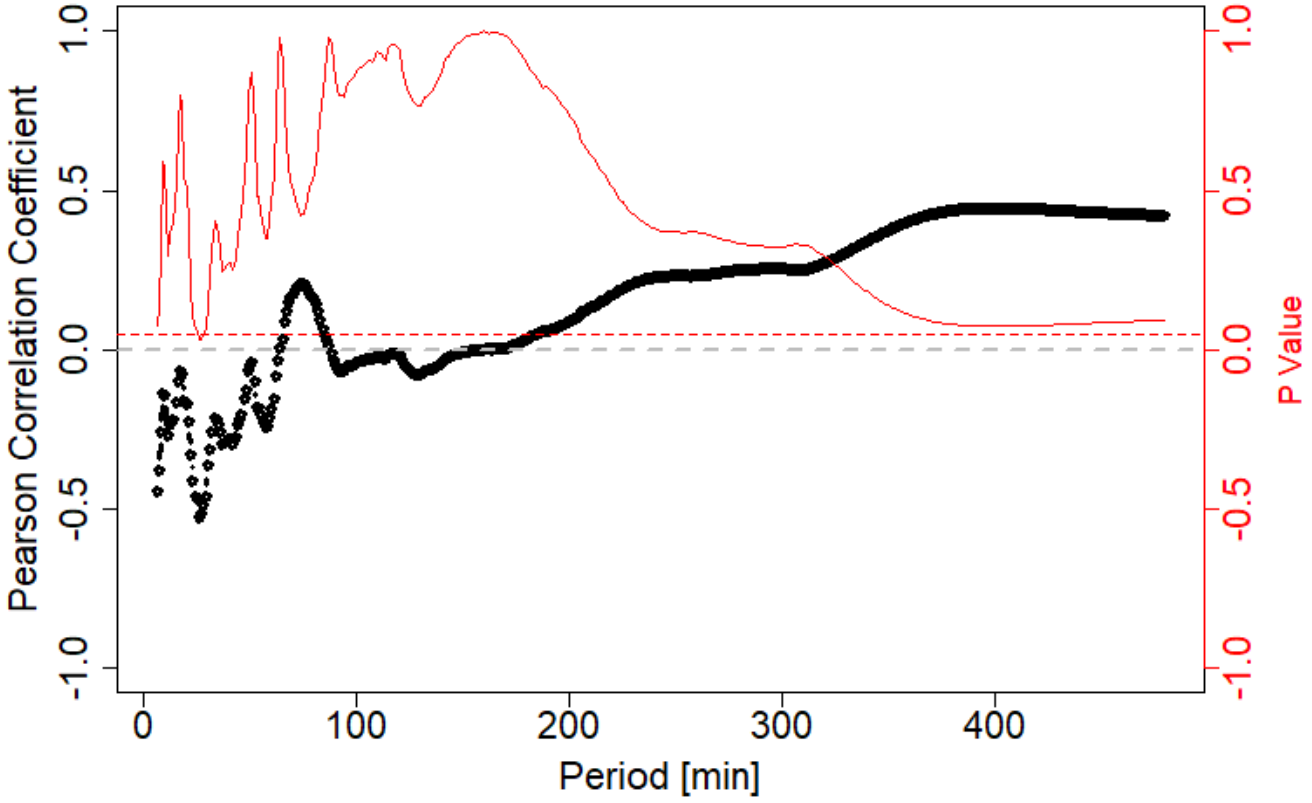

735 **Figure 7~~7~~. Pearson correlation coefficient (black) between gravity wave activity (SWI) from GRIPS data and eddy diffusion coefficients from FAIM 3 data above OTL. The P value is plotted in red. For all P values of 0.05 (red horizontal line) or ~~equal~~ less the correlation coefficient is considered significant. ~~A significant anticorrelation between SWI and the eddy diffusion coefficient is found between periods of 122 min and 207 min (grey vertical lines).~~**

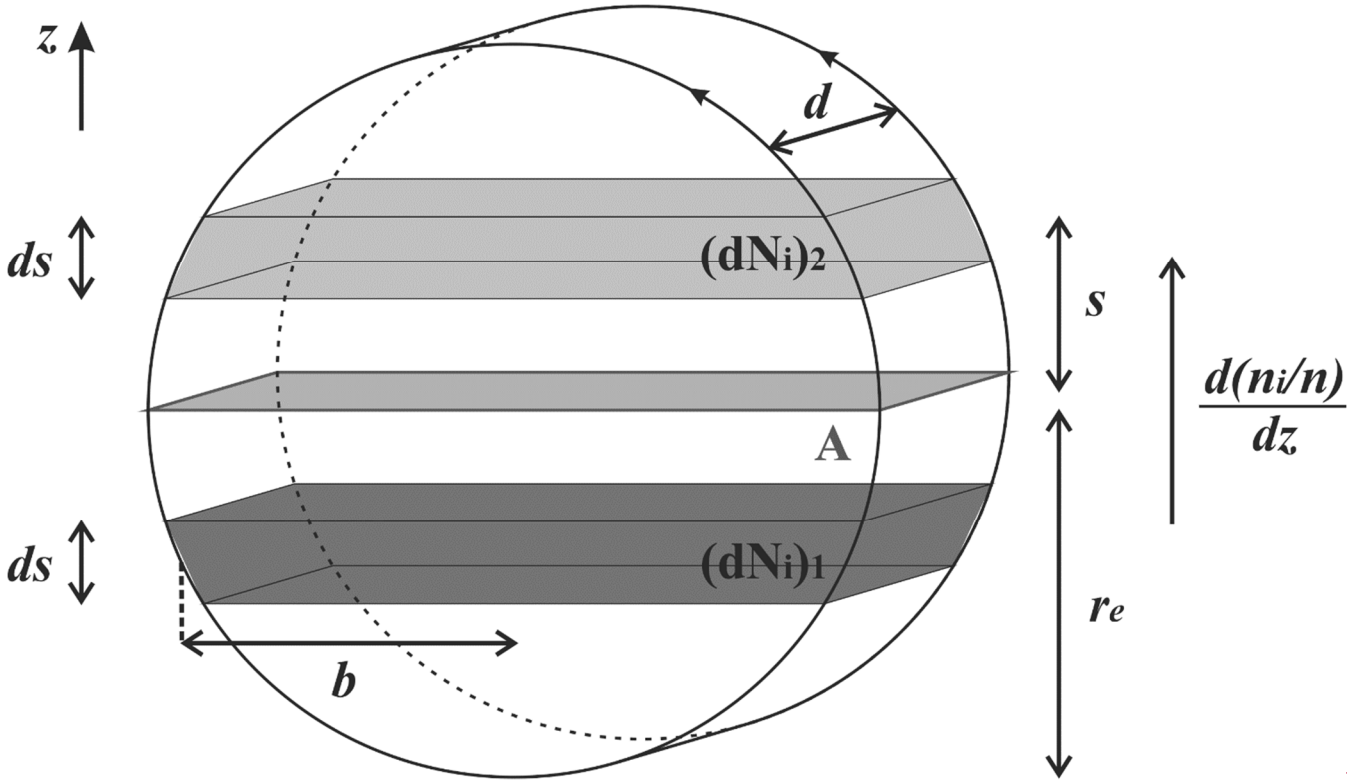

740 ~~Figure 8. Concept of cylindrical mixing according to Prölss (2001). Description in text.~~

Tables

Table 1. Episodes of turbulence observed at OTL and derived parameters from the image sequences. The BV frequency is according to the climatology based on TIMED-SABER measurements as presented by Wüst et al. (2020). The duration of the turbulence events could not be determined if the vortex was not visible during its entire life span due to being partly outside the FOV ('out of FOV') of FAIM 3 or covered by clouds ('clouds'). In these cases, we noted the dissipated energy per mass and the maximum temperature change as 'not available' (NA).

Date	DoY [d]	K [10^4 m^2/s]	Duration [s]	Angular BV frequency [10^{-2} 1/s]	ϵ [W/kg]	Diss. energy per mass [J/kg]	Max. temperature change [K]
2017-10-30	303	0.38 ± 0.08	out of FOV	2.10 ± 0.11	2.07 ± 0.63	NA	NA
2017-10-30	303	1.07 ± 0.13	244	2.10 ± 0.11	5.82 ± 1.31	1420 ± 319	1.4 ± 0.3
2017-11-01	305	0.27 ± 0.07	388	2.10 ± 0.11	1.48 ± 0.56	575 ± 217	0.6 ± 0.2
2017-11-16	320	0.17 ± 0.05	241	2.09 ± 0.10	0.91 ± 0.38	220 ± 92	0.2 ± 0.1
2017-11-18	322	0.54 ± 0.09	546	2.09 ± 0.10	2.90 ± 0.80	1585 ± 434	1.6 ± 0.4
2017-12-05	339	1.36 ± 0.15	373	2.09 ± 0.10	7.32 ± 1.56	2730 ± 583	2.7 ± 0.6
2017-12-06	340	0.33 ± 0.08	922	2.09 ± 0.10	1.79 ± 0.61	1655 ± 565	1.7 ± 0.6
2017-12-09	343	0.24 ± 0.08	407	2.09 ± 0.10	1.30 ± 0.57	530 ± 233	0.5 ± 0.2
2017-12-09	343	0.91 ± 0.13	390	2.09 ± 0.10	4.94 ± 1.20	1925 ± 469	1.9 ± 0.5
2018-01-22	22	0.84 ± 0.12	387	2.08 ± 0.10	4.53 ± 1.11	1752 ± 430	1.8 ± 0.4
2018-02-05	36	0.70 ± 0.11	146	2.07 ± 0.10	3.69 ± 0.93	538 ± 135	0.5 ± 0.1
2018-03-24	83	1.56 ± 0.16	250	2.11 ± 0.11	8.61 ± 1.75	2153 ± 437	2.2 ± 0.4
2018-04-12	102	0.70 ± 0.11	252	2.19 ± 0.11	4.16 ± 1.04	1048 ± 262	1.0 ± 0.3
2018-04-21	111	1.69 ± 0.17	292	2.23 ± 0.11	10.36 ± 2.08	3026 ± 608	3.0 ± 0.6
2018-04-29	119	0.96 ± 0.13	458	2.27 ± 0.11	6.09 ± 1.41	2787 ± 645	2.8 ± 0.6
2018-05-02	122	0.26 ± 0.08	531	2.28 ± 0.11	1.70 ± 0.67	905 ± 358	0.9 ± 0.4
2018-05-20	140	1.05 ± 0.13	out of FOV	2.37 ± 0.12	7.26 ± 1.64	NA	NA
2018-05-31	151	0.16 ± 0.06	309	2.42 ± 0.12	1.13 ± 0.55	349 ± 169	0.3 ± 0.2
2018-06-02	153	0.47 ± 0.09	413	2.42 ± 0.12	3.39 ± 1.00	1401 ± 414	1.4 ± 0.4
2018-06-04	155	0.22 ± 0.06	677	2.43 ± 0.12	1.63 ± 0.62	1102 ± 418	1.1 ± 0.4
2018-06-16	167	0.20 ± 0.06	291	2.46 ± 0.12	1.50 ± 0.58	437 ± 170	0.4 ± 0.2
2018-06-18	169	0.32 ± 0.15	382	2.47 ± 0.12	2.38 ± 1.11	908 ± 423	0.9 ± 0.4
2018-07-04	185	0.40 ± 0.08	340	2.48 ± 0.12	3.05 ± 0.94	1039 ± 320	1.0 ± 0.3
2018-07-25	206	0.33 ± 0.13	out of FOV	2.44 ± 0.12	2.42 ± 1.21	NA	NA
2018-07-28	209	1.94 ± 0.18	444	2.44 ± 0.12	14.21 ± 2.78	6309 ± 1233	6.3 ± 1.2
2018-09-21	264	1.90 ± 0.19	out of FOV	2.20 ± 0.11	11.34 ± 2.25	NA	NA

2018-09-21	264	0.13 ± 0.11	out of FOV	2.20 ± 0.11	0.78 ± 0.69	NA	NA
2018-10-02	275	0.23 ± 0.08	out of FOV	2.16 ± 0.11	1.31 ± 0.62	NA	NA
2018-10-04	277	0.59 ± 0.10	276	2.15 ± 0.11	3.38 ± 0.90	932 ± 248	0.9 ± 0.2
2018-10-04	277	0.86 ± 0.12	345	2.15 ± 0.11	4.95 ± 1.17	1709 ± 405	1.7 ± 0.4
2018-10-13	286	1.24 ± 0.15	914	2.13 ± 0.11	6.94 ± 1.50	6346 ± 1375	6.3 ± 1.4
2018-10-14	287	1.35 ± 0.16	out of FOV	2.13 ± 0.11	7.55 ± 1.63	NA	NA
2018-11-04	308	1.23 ± 0.15	915	2.09 ± 0.10	6.66 ± 1.45	6097 ± 1331	6.1 ± 1.3
2018-11-04	308	0.30 ± 0.08	609	2.09 ± 0.10	1.61 ± 0.61	983 ± 372	1.0 ± 0.4
2018-11-08	312	0.68 ± 0.10	out of FOV	2.09 ± 0.10	3.69 ± 0.93	NA	NA
2018-11-08	312	0.55 ± 0.09	out of FOV	2.09 ± 0.10	2.99 ± 0.80	NA	NA
2018-11-16	320	0.12 ± 0.12	out of FOV	2.09 ± 0.10	0.63 ± 0.70	NA	NA
2018-11-16	320	0.92 ± 0.13	292	2.09 ± 0.10	4.97 ± 1.19	1450 ± 346	1.4 ± 0.3
2019-01-11	11	0.57 ± 0.11	421	2.10 ± 0.11	3.08 ± 0.93	1297 ± 392	1.3 ± 0.4
2019-02-22	53	1.07 ± 0.14	318	2.07 ± 0.10	5.64 ± 1.28	1794 ± 409	1.8 ± 0.4
2019-02-24	55	1.61 ± 0.16	out of FOV	2.07 ± 0.10	8.51 ± 1.70	NA	NA
2019-03-02	61	1.69 ± 0.17	306	2.07 ± 0.10	8.95 ± 1.77	2739 ± 543	2.7 ± 0.5
2019-03-30	89	0.31 ± 0.11	453	2.13 ± 0.11	1.75 ± 0.80	793 ± 364	0.8 ± 0.4
2019-04-07	97	1.28 ± 0.17	clouds	2.17 ± 0.11	7.39 ± 1.72	NA	NA
2019-05-09	129	0.39 ± 0.13	out of FOV	2.32 ± 0.12	2.56 ± 1.14	NA	NA

Date	ϵ [W/kg]	Duration [s]	Diss. energy per mass [J/kg]	Max. temperature change [K]
2017-10-30	5,39 ± 1,55	out of FOV	NA	NA
2017-10-30	0,16 ± 0,16	244	38,12	0,04
2017-11-16	1,80 ± 0,76	241	434,82	0,43
2017-11-18	0,29 ± 0,22	546	158,92	0,16
2017-12-06	0,40 ± 0,29	922	368,90	0,37
2017-12-09	5,07 ± 1,46	407	2062,35	2,06
2017-12-09	0,14 ± 0,11	390	54,62	0,05
2018-01-22	1,45 ± 0,70	387	560,42	0,56
2018-04-13	0,58 ± 0,37	252	146,24	0,15
2018-05-02	0,57 ± 0,33	531	305,22	0,31

2018-05-20	2,63 ± 1,04	out of FOV	NA	NA
2018-06-04	0,37 ± 0,26	677	253,44	0,25
2018-06-16	2,61 ± 1,04	291	760,87	0,76
2018-07-28	5,97 ± 1,70	444	2651,59	2,65
2018-09-21	0,80 ± 0,41	out of FOV	NA	NA
2018-10-04	0,09 ± 0,08	345	29,87	0,03
2018-10-14	9,03 ± 2,67	out of FOV	NA	NA
2018-11-04	3,30 ± 1,03	915	3015,28	3,02
2018-11-04	0,62 ± 0,33	609	378,88	0,38
2018-11-08	7,91 ± 2,00	out of FOV	NA	NA
2018-11-16	5,24 ± 1,45	out of FOV	NA	NA
2019-01-11	0,69 ± 0,40	421	289,10	0,29
2019-02-22	0,10 ± 0,12	318	31,13	0,03
2019-02-24	8,02 ± 1,66	out of FOV	NA	NA
2019-04-07	1,67 ± 0,72	clouds	NA	NA